Energy & Buildings 298 (2023) 113540

Contents lists available at ScienceDirect

Energy & Buildings

journal homepage: www.elsevier.com/locate/enb

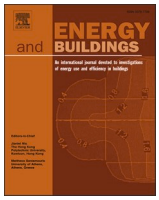

Assessing heat transfer characteristics of building envelope deployed BIPV and resultant building energy consumption in a tropical climate

Hamza Jhumka [a], Siliang Yang [a,*], Christopher Gorse [b], Sara Wilkinson [c], Rebecca Yang [d], Bao-Jie He [e,f,g,h], Deo Prasad [i], Francesco Fiorito [i,j]

[a] School of Built Environment, Engineering and Computing, Leeds Beckett University, Leeds, United Kingdom
[b] School of Architecture, Building and Civil Engineering, Loughborough University, Loughborough, United Kingdom
[c] School of Built Environment, University of Technology Sydney, Sydney, Australia
[d] School of Property, Construction and Project Management, RMIT University, Melbourne, Australia
[e] Centre for Climate-Resilient and Low-Carbon Cities, School of Architecture and Urban Planning, Chongqing University, Chongqing, China
[f] Network for Education and Research on Peace and Sustainability (NERPS), Hiroshima University, Hiroshima, Japan
[g] Key Laboratory of New Technology for Construction of Cities in Mountain Area, Ministry of Education, Chongqing University, Chongqing, China
[h] State Key Laboratory of Subtropical Building Science, South China University of Technology, Guangzhou, China
[i] School of Built Environment, University of New South Wales, Sydney, Australia
[j] Department of Civil, Environmental, Land, Building Engineering and Chemistry, Polytechnic University of Bari, Bari, Italy

ARTICLE INFO

Keywords:
BIPV glazing
Roof BIPV membrane
Double-skin façade
Heat transmission
Thermal impact
Cooling load

ABSTRACT

Building-Integrated Photovoltaic (BIPV) is a viable technology towards increasing renewable energy production and achieving low carbon footprints for buildings. Mauritius, with a daily average of 5.6 kWh/m^2 of solar radiation over 2350 h annually, has been targeting at achieving its low carbon goals by focusing on photovoltaic technology including the uptake of BIPV. However, BIPV has not been well researched in terms of its overall thermal impact especially overheating on the building envelope and the resultant energy performance for buildings for the tropical climatic condition in Mauritius. This research, by means of validated simulation modelling, adopted a novel approach of coupling thermal finite element analysis (FEA) with whole building dynamic simulations to assess the heat transfer characteristics of BIPV either on facades or roof and the resultant energy consumptions of a typical office building in Mauritius. The façade scenario had two options, namely BIPV curtain wall and BIPV double-skin façade (BIPV-DSF), while the roof scenario also had two options, namely uninsulated and insulated roof BIPV membranes. Results show that roof BIPV membrane options had a better thermal performance in reducing overheating for the building compared to the BIPV façade options, with a reduction in cooling load of 8% and 15% for the uninsulated and insulated BIPV membranes, respectively. In terms of energy performance, both BIPV façade options were not capable of reducing the energy consumption of the building, as the BIPV curtain wall resulted in 1.66% more net energy consumption on a yearly basis. This shows an ineffectiveness of using vertical BIPV glazing for typical office buildings in Mauritius. Although the BIPV-DSF achieved an annual net energy saving of 5.16% benefited from the BIPV energy production, it was not as good as the net savings of 160% and 172% from the respective uninsulated and insulated roof BIPV membrane options.

1. Introduction

Global warming is one of the major issues that needs to be tackled by countries worldwide, with a target of keeping the warming effect below 1.5 °C over the next two decades as a generally accepted consensus [1]. This warming effect, led by one of the main culprits that the energy sector with energy generation through fuel and coal power stations, is being a major catalyst of greenhouse gases in our atmosphere [2–4]. As such, it can be deduced that global warming is a by-product of energy consumption. Buildings are amongst the biggest energy consumers worldwide, and reducing the energy demand of buildings can lower their carbon emission footprint and help reduce the effect of global warming [5,6].

* Corresponding author.
E-mail address: s.yang@leedsbeckett.ac.uk (S. Yang).

https://doi.org/10.1016/j.enbuild.2023.113540
Received 26 May 2023; Received in revised form 17 August 2023; Accepted 11 September 2023
Available online 14 September 2023

Nomenclature

Symbols

A_i	inside surface area [m^2]
C_p	specific heat capacity [J/kgK]
h	convective heat transfer coefficient [W/m^2K]
h_{ext}	external surface convective heat transfer coefficient [W/m^2K]
h_i	internal surface convective heat transfer coefficient [W/m^2K]
h_{int-h}	internal surface (horizontal) convective heat transfer coefficient [W/m^2K]
h_{int-v}	internal surface (vertical) convective heat transfer coefficient [W/m^2K]
I	current in one-diode equivalent circuit [A]
I_L	photovoltaic module photocurrent [A/W]
I_{mpp}	current at maximum output [A]
I_o	diode reverse saturation current [A]
I_s	incident solar radiation on solar cell surface [W/m^2]
I_{sc}	short circuit current of photovoltaic module [A]
i	instance of study [-]
k	thermal conductivity [W/mK]
k	Boltzmann's constant [J/K]
M_i	measured data [-]
$\overline{M_P}$	average of measured data [-]
$\dot{m}_i$	interzone air mass flow rate [kg/h]
$\dot{m}_{inf}$	outside air mass flow rate due to infiltration [kg/h]
$\dot{m}_{sys}$	supply air mass flow rate [kg/h]
n	total number of data samples [-]
N_P	number of values for a given time duration [-]
P	calculation time interval [-]
P_{mpp}	maximum power of photovoltaic module [W_p]
Q	heat flux [W/m^2]
Q_{D-Tr}	directly transmitted heat flux [W/m^2]
Q_{elec}	converted electric power [W/m^2]
Q_{ETFE}	heat flux through ethylene tetrafluoroethylene layer [W/m^2]
Q_{EVA}	heat flux through ethylene–vinyl acetate layer [W/m^2]
Q_{float}	heat flux through float glass layer [W/m^2]
Q_{glass}	heat flux through low iron glass layer [W/m^2]
Q_{PV}	heat flux through photovoltaic module layer [W/m^2]
Q_{PVB}	heat flux through polyvinyl butyral layer [W/m^2]
$Q_{reflect}$	reflected heat flux [W/m^2]
Q_{solar}	irradiance on solar cell surface [W/m^2]
$\dot{Q}_i$	internal load [kW]
$\dot{Q}_{load}$	net zone thermal load [kW]
$\dot{Q}_{sys}$	air system thermal load [kW]
q	elementary charge [C]
R_s	photovoltaic module series resistance [Ω]
S_i	simulated data [-]
T	local temperature [K]
T_a	ambient air temperature [K]
T_{air}	external or internal air temperature [K]
T_c	photovoltaic cell temperature [K] [K]
T_{ext}	external air temperature [K]
T_{int}	internal air temperature [K]
T_{PV}	photovoltaic module temperature [K]
T_{si}	internal surface temperature [K]
T_{sup}	supply air temperature [K]
T_{surf}	surface temperature [K]
T_z	zone mean air temperature [K]
T_{zi}	interzone air temperature [K]
T_∞	outside air temperature [K]
t	time taken [s]
U-value	heat transfer coefficient or thermal transmittance [W/m^2K]
V	voltage in one-diode equivalent circuit [V]
V_{mpp}	voltage at maximum output [V]
V_{oc}	open circuit voltage of photovoltaic module [V]
x_i	calculated value [-]
y_i	simulated value [-]

Greek symbols

γ	empirical photovoltaic curve-fitting parameter [-]
ε	emissivity of surface being subject to radiant energy [-]
ε_{ext}	emissivity of external surface [-]
ε_{int}	emissivity of internal surface [-]
ρ	density [kg/m^3]
σ	Stefan-Boltzmann constant [W/m^2K^4]

Abbreviations

ACH	air changes per hour
a-Si	amorphous silicon
BAPV	building-attached photovoltaic
BIPV	building-integrated photovoltaic
BIPV-DSF	building-integrated photovoltaic in double-skin facade
CdS	cadmium sulphide
CdTe	cadmium telluride
CIGS	copper indium gallium selenide
CVRMSE	cumulative variation of root mean squared error
DSF	double-skin facade
DSSC	dye-sensitised solar cell
DX	direct expansion
ETFE	ethylene tetrafluoroethylene
EVA	ethylene–vinyl acetate
FEA	finite element analysis
HVAC	heating, ventilation, and air conditioning
MBE	mean bias error
NOCT	nominal operating cell temperature
OPV	organic photovoltaic
PIR	polyisocyanurate
PSC	perovskite solar cell
PV	photovoltaic
PVB	polyvinyl butyral
PVC-P	plasticised polyvinyl chloride
RRMSE	relative root mean square error
SHGC	solar heat gain coefficient
TPT	Tedlar Polyester Tedlar
VLT	visible light transmittance

Mauritius recently embarked on several ambitious journeys, first with the "Smart City Scheme" to promote the construction of smart cities around the island, and at the same time adopt a low carbon strategy to keep up with the United Nations climate change policies agreed at the COP26 [7,8]. The target is to achieve carbon neutrality by 2070 along with an intermediate goal of generating 40% of its energy through renewables by 2030 [8]. Whilst adoption of the Smart City Scheme would lead towards more construction of mid- to high-rise buildings that require more electrical energy [9], the climate change mitigation measure of Net Zero Carbon will force the building and construction sector towards a more sustainable and low energy approach during design, construction, and operation [10]. Khoodaruth et al. [11] conclude that the participation of the Mauritian policy makers and regulators are fundamental along with public sensitisation and financial investments

towards decarbonising the energy systems through 100% renewable energy by 2050 for the country.

Solar energy is one of the most widely adopted renewable energy sources to increase sustainability in most sectors including building and construction [12]. With Mauritius receiving a daily average of 5.6 kWh/m^2 of solar radiation over an average of 2350 h annually, solar energy is one of the most viable options in terms of renewable source [11]. The United Nations Development Programme (UNDP) with the support of the Green Climate Fund has been assisting Mauritius in achieving its 2030 Renewable Energy Roadmap by focusing on solar photovoltaic (PV) technology [13]. Ramgolam and Soyjaudah [14], while studying the potential of PV systems, found that Mauritius could yield an average of 1428 kWh/m^2 of solar energy per year. While the PV system has an encouraging future as a sustainable and renewable energy technology, the main barrier to its implementation is physical space [15]. On-site solar farms for individual buildings can take a considerable amount of space, while being aesthetically unpleasant and being an unwanted source of glare [16]. Since the 2000 s, an innovative form of PV systems has been developed and implemented globally, namely building-integrated photovoltaic (BIPV). This system which uses PV arrays integrated into the building envelope can form a cohesive design, construction, and energy solution for buildings [17]. Several studies such as Biyik et al. [18], Yu et al. [19] and You and Yang [20] reviewed and showed the encouraging potential of BIPV as energy generators, while Shukla et al. [21] gave an indication of the lifecycle assessment showing a reasonable economic payback and carbon footprint reduction of BIPV in general.

On the other hand, solar radiation that reaches the BIPV arrays is partly absorbed by the building envelope itself [22]. The absorbed heat travels through convection, if there is a gap between the arrays and the building envelope, then it travels by conduction and radiation to the internal surface of the building to be transmitted to the indoor space thermal load [23]. However, very little research has assessed the heat transfer characteristics of BIPV on building envelopes and its impact on the cooling load of buildings [19]. Most existing research is limited to analysing PV module surface temperatures and the impact of solar transmission from glazed BIPV options even though BIPV glazing makes up only 20% of the current market [21]. Therefore, this paper presents research aimed at investigating the comparative thermal impact of both roof and glazed type BIPVs on the indoor air temperature of a typical office building situated in the tropical climate of Mauritius. The BIPV heat transmission will then be integrated into energy models to assess the overall effect of this heat gain on the energy consumption of the building and the resultant energy savings due to the energy production of the BIPV.

In summary, this paper is subdivided into 6 sections, namely introduction, literature review, materials and methods, model calibration, results and discussion, and conclusion. The introduction section gives insight on the background information leading to the research motivation. Literature review covers the current studies with respect to energy and thermal impact of BIPV on buildings, where a problem statement concludes the review with clear guidelines on the significance of this research. The section of materials and methods provides an overview of the methodology including a description of the case study with the input parameters. Model calibration shows the calibration procedure of validating the simulation model. Results and discuss section presents the numerical results obtained and the findings of this study. Finally, the section of conclusions restates the research conducted and summarises the main findings with a critical insight on the key metrics from the analysis.

2. Literature review

2.1. Overview of BIPV

PV modules come in several configurations namely framed, unframed, roof tiles or a building component itself [24]. There are modules which are either opaque, or semi-transparent, that are mounted on structural frames, or between glass panels to be fixed as glazing components on a building [25]. When they are integrated into the building structure they are known as BIPV, whereas if they are fixed onto a building component or structure then they are known as Building Attached Photovoltaic (BAPV) [26]. Without knowledge of the mounting system used, it is difficult to differentiate between the two since PV arrays constitute most of the visible portion in both cases. The BAPVs have no significant effect on the functionality of the envelope of a building, the BIPVs however, will have a direct impact on the envelope, as it is replacing a specific building component and; is a fundamental variable parameter for the energy balance of the building [18].

The CIBSE (Chartered Institution of Building Services Engineers) Knowledge Series KS15 [25] indicates that there are two types of BIPV systems, namely roof-integrated and façade-integrated, by providing a list of sub-classifications for both. The façade-integrated type is categorised as vertical curtain walling, inclined wall glazing, rain-screen cladding and sun shading, while the roof-integrated type is categorised as inclined roof, curved roof, skylights, and atrium. It should be noted that the roof-mounted systems are usually placed on a structural roof and considered as BAPV. It is stated that the roof-integrated system provides for the better energy performance, while the façade-integrated has more opportunities to be used as a secondary function such as rain screen or sun shading while providing for an architectural statement [25]. Being transparent, the façade installations also provide for more daylighting capabilities [27,28]. Yu et al. [19] further categorised the glazing-mounted BIPV into four distinct types, namely single layer, double-layer with closed air gap, double-layer with a ventilated air gap and vacuum type, while the last one had the lowest heat transfer rate as low as 0.6 W/m^2K under the influence of solar irradiation. The double-layer PV also had low heat transmission at almost the same magnitude as the vacuum type, but the single layer PV had the highest heat transmission with a rate as high as 5.5 W/m^2K for certain solar cell materials. They indicate that there is lack of research on the double-layer and vacuum types compared to the single layer type to provide for a more impartial assessment of their heat transfer capabilities and energy performance.

2.2. BIPV material and its applications in buildings

Three main types of BIPV material are monocrystalline silicon, polycrystalline silicon, and thin-film coating [29], while some lesser used materials are the non-silicon versions such as dye-sensitised solar cell (DSSC), perovskite solar cell (PSC) and organic photovoltaic (OPV) [30]. Monocrystalline silicon is the most efficient type, but also the most expensive one, due to being made from a slice of a single crystalline silicon, while polycrystalline, which has larger cells, is made from multi-crystalline silicon cast in a mould [31]. Thin-film is a micron sized coating made of cadmium sulphide (CdS), cadmium telluride (CdTe) and amorphous silicon (a-Si), which is used on a variety of substrates ranging from glass to steel [30]; although it is the least efficient, layering two or more thin-film PV junctions on top of each other can improve the performance both in electricity conversion efficiency and reduction of mechanical degradation over time [32,33]. Research has shown the potentialities of using thin-film based BIPV on building envelopes in terms of its thermal and energy performance [34,35].

Some studies revealed the availability and feasibility of BIPV application in different parts of the building envelope. Shukla et al. [21] conclude the recent technologies classifying BIPV installations into tiling products for roofs, glazing products for both roofs and façades, foil products for curved roofs, and other products for shading and cladding materials. They found that 80% of the current market is dominated by the roof-mounted BIPV, using both glazed semi-transparent materials and opaque tiling materials, while the façade-mounted installations only account for 20% of the market. Shukla et al. [21] also indicate that the

payback period for both installations with monocrystalline requiring around 2.7 to 7.3 years, while thin-film costs could be recovered within the first 8 months to 4 years at most. Previously, by surveying the European market, Pester [36] found that monocrystalline was the most used PV cell for the opaque application such as roof tiles, slates and frameless laminates, while the thin-film was used mostly for the semi-transparent glazing for windows, skylights and curtain walls.

Furthermore, the thin coating consisting of copper indium gallium selenide (CIGS) photovoltaic cells are used on lightweight metal roofing also as a BIPV [37]. The foil type, which uses a-Si combined with other cushioning structural material such as ethylene tetrafluoroethylene (ETFE), comes in the form of rolls and membranes that are used on roof surfaces by simple adhesion without the need for frames or mounting elements [38]. Those flexible BIPV modules can take the shape of the roof structure including the curved roof [30].

2.3. Bipv-induced thermal impact on buildings

BIPVs are normally analysed through their electricity generation efficiency noted by energy production and their thermal performance through the heat transfer coefficient; commonly known as the U-value [39]. When BIPV is transparent, or semi-transparent (glazed type), its thermal performance includes the solar heat gain coefficient (SHGC) which informs of the solar irradiation transmitted through the PV media into the building [40]. Another performance factor normally involved when dealing with glazed BIPV is the optical performance measured through the visible light transmittance (VLT) and the glare probability value to assess the indoor visual effects [19,40,41], while an acceptable daylighting can be maintained when the VLT is within the range of 25% – 38% [42,43].

A comprehensive literature review by Maghrabie et al. [30] concluded that semi-transparent thin-film PV modules have superior performance levels with their capabilities to produce electricity while reducing the cooling load through the partial absorption of solar radiation incident on the envelope. However, most of the research was based on the PV modules with a façade integration, and few of them were compared to roof-mounted systems [44]. Earlier, Ban-Weiss et al. [22] provided an analysis of a roof-integrated BIPV consisting of thin-film a-Si noting a 5 °C decrease on the upper surfaces, as a result of the increased solar absorption and a 9.6 kWh/m^2 reduction on the cooling load; however, the BIPV used for the research is no longer available on the PV market and further research is needed to update the present roof-mounted thin-film BIPV.

In comparison, it was found that a crystalline PV module can convert around 15–20% of incident irradiation into electrical energy, while another 5–10% are reflected, or converted, into other energy sources [30,45]. This could allow the BIPV modules to yield a surface temperature of 60 °C on hot and sunny days, which warrants the need for ventilated gaps between the BIPV and building envelope to provide a thermal break in the energy transfer [30].

In recent years, Yang et al. [43,46–48] numerically analysed the effect of a-Si, DSSC and PSC based BIPVs combined with a ventilated double-skin façade (DSF) in Australian climate, which found that the ventilated air gap produced energy savings from 34% up to 106% depending on the region due to the heat harvesting capabilities of the air gap. They also demonstrated that the heat recovery combined with the electricity generated would potentially offset the energy demand due to additional heat gains on the envelope [46], while the ventilated DSF with BIPV could be beneficial to improvement of indoor thermal comfort in summertime [43,48].

A numerical study through EnergyPlus simulation in Cameroon's tropical climates earlier showed an increase in the indoor temperature by 4 °C using BIPV, while the type of BIPV adopted was not specified [49]. The authors found that roof-integrated BIPV had a considerable impact on the indoor hygrometric conditions than façade applications. However, the study did not incorporate the indoor heat gains and HVAC (heating, ventilation, and air conditioning) in the assessment.

By using a high reflectivity heat insulation film laminated with a varied combination of thin-film semi-transparent PV modules of a-Si, Liu et al. [50] discovered an average of 34.2% energy savings on the HVAC in sub-tropical climate of Taiwan due to the low SHGC and low U-value achieved from the insulation. They also found a visible light reflectance of only 5% using the insulation film, hence the impact on the visual performance, or light pollution, of the glazed PV was negligible. In terms of a DSF variation to a semi-transparent a-Si thin-film glazing, Han et al. [51] determined that a ventilated gap in the PV module would provide a reduction of cooling load in subtropical climates. However, they only analysed temperature profiles with respect to energy generating capacities of the BIPV without an actual analysis of the effects on cooling loads.

2.4. Problem statement

Even though literature has shown that thermal and energy performance evaluation for BIPV is a well-documented research topic, there are considerable ambiguities about the thermal gains and subsequent impact on energy savings, which makes the assessment of BIPV for the Mauritian climate a difficult task. Mauritius has a cooling only climate [52], while the energy savings stated in the literature are often a result of the impact of BIPV on space heating. Several factors, such as local codes, construction practices and socio-economic contexts may also affect the impact of BIPV on local buildings [53]. Although thermal aspects are present in current literature, the impact of BIPV installation on the cooling load of a building has not been researched.

This paper proposes a novel approach of assessing the thermal performance of a semi-transparent BIPV glazing and a roof BIPV membrane on buildings in Mauritius, using a case study of a typical office building to analyse cooling load variations in the tropical climate of the country and correlating the thermal performance to energy harvesting capabilities of the BIPV for an overall energy assessment. The significance of the proposed research will provide a basis for the building professionals to assess the thermal impact and energy performance of BIPV on buildings in a broader tropical climate context such as the hidden problem of overheating.

3. Materials and methods

This research aimed to investigate two types of BIPV materials on the fabric of a case study building in Mauritius. Since the case study building is existing and operational, a real retrofit is not economically feasible. Thus, the research was essentially based on calibrated simulations for a comparative study. The study comprised two areas – thermal performance and energy performance analyses. The thermal analysis consisted of a detailed finite element heat transfer analysis and a dynamic building performance analysis. Specifically, the finite element heat transfer analysis was used to predict thermal performance of the selected BIPV materials, while the dynamic building performance simulation was used to analyse the thermal impacts of the BIPV on the building cooling load. On the other hand, the energy performance analysis consisted of an energy modelling of the building usage and PV energy generation, which assesses the whole building energy performance through parametric scenarios.

3.1. BIPV typologies

Literature showed the typical typologies of BIPV in the built environment. This research focused on analysing three main typologies as follows:

1) A flat roof based waterproofing BIPV membrane.
2) A façade based glazed BIPV curtain wall.

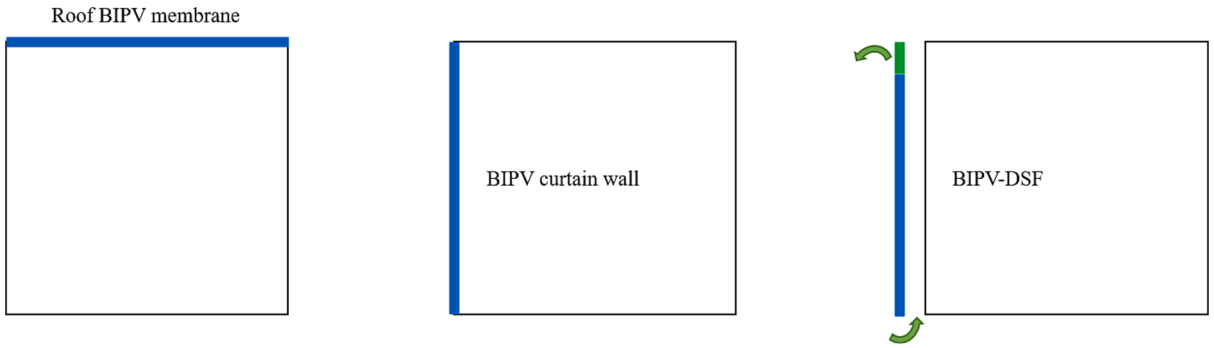

Fig. 1. Typologies of BIPV models for analysis: roof BIPV membrane (left), BIPV curtain wall (middle), and naturally ventilated DSF with semi-transparent BIPV glazing (right). The blue colour of the schematics represents the BIPV structure. (For interpretation of the references to colour in this figure legend, the reader is referred to the web version of this article.)

Fig. 2. The case study building – a view of south-west façade.

3) A naturally ventilated DSF comprising of a front layer of semi-transparent BIPV glazing (also known as building-integrated photovoltaic in double-skin façade, shortened to BIPV-DSF).

Fig. 1 illustrates the typologies and building surfaces of the case study that were substituted with the selected BIPV material for the numerical simulations in assessing the thermal load variations of the building.

3.2. Ansys modelling – Thermal performance of BIPV

Ansys is a multi-physics finite element analysis (FEA) programme being widely used in both commercial and academic settings, which has different packages that can numerically model and solve static and dynamic heat transfer and fluid problems [54]. The package used in this research was Ansys Mechanical, which performed steady state finite element heat transfer analysis for the individual BIPV materials. Ansys Mechanical is a new approach towards BIPV analysis, but it has been commonly used to analyse regular PV modules [55–57].

3.3. DesignBuilder modelling – Energy performance of BIPV

DesignBuilder is a whole building dynamic simulation software that provides a graphical user interface to the EnergyPlus simulation engine. The typical workflow consists of the selection of a location and corresponding weather data, the creation of the thermal building model geometry and assigning occupancy and equipment operation schedules; the results range from thermal load profiles to lighting illumination profiles and other energy simulation data [58]. DesignBuilder is used mainly to evaluate façade options, daylighting analysis, visualisation of site layouts and solar shading, thermal conditions, and the sizing of HVAC equipment and systems [59]. A number of studies have successfully validated the thermal and energy performance simulation capabilities of DesignBuilder [60–62].

Table 1
Case study building features.

Type of features	Parameters	Details
Climate features	Location	Pointe aux Canonniers, Mauritius
	Climate classification	Tropical monsoon climate
Architectural features	Total building floor area	2003 m^2
	Façade area	354 m^2
	Façade glazing area	172 m^2
Mechanical features	Cooling system only	Direct Expansion (DX) coil split system
	Energy for building operation	Electricity
	Conditioned area	1712 m^2
	Unconditioned area	291 m^2

3.4. Case study building overview

The case study building is a typical office building located in Pointe aux Canonniers, the north-west of Mauritius (as shown in Fig. 2). It has around 471 m^2 space area per floor over three floors, of which both the ground floor and first floor have a mezzanine having roughly 60% floor space and 40% open space. The building height is 14.8 m, and it has a glazed façade oriented towards the south-west. Due to the building being in the Southern Hemisphere, the glazed façade is oriented towards the south to limit heat gains in the building.

The building features are given in Table 1, while Fig. 3 shows the south-west elevation of the façade with its curtain wall at ground floor level and large glazed windows on the remaining floors, as well as a typical floor layout with its mezzanine. The building is used as an office with common circulation areas and customary wet areas. The building envelope consists primarily of lightweight 200 mm concrete blocks with cast-in-place concrete columns, beams and slabs for the structural elements. The curtain wall and façade windows are double glazed 6 mm glass with a 12 mm air gap.

3.5. Development of numerical modelling

3.5.1. Finite element heat transfer modelling

Heat transfer is energy transfer between material bodies due to temperature differences; the governing equations used for finite element steady state heat transfer analysis is derived from the first law of thermodynamics for the conservation of energy [63] as follows:

$$Q_{conduction} + Q_{convection} + Q_{radiation} = \rho C_p \frac{dT}{dt} \quad (1)$$

Where Q is the heat flux (in conduction, convection, and radiation), ρ is the density of a material, C_p is the specific heat capacity of the material, $\frac{dT}{dt}$ is the temperature change with time taken as 1 s for a steady state calculation.

Specifically, heat transfer through conduction is given by Fourier's law as:

$$Q_{conduction} = -k\frac{dT}{d\Delta} \quad (2)$$

Where k is the thermal conductivity of the material, $\frac{dT}{d\Delta}$ is the temperature gradient occurring in ×, y, and z directions.

The convective heat transfer is given by Newton's law of cooling as:

$$Q_{convection} = h(T_{surf} - T_{air}) \quad (3)$$

Where h is the convective heat transfer coefficient in relation to air movement, T_{surf} is the surface temperature in contact with air, T_{air} is the external or internal air temperature.

Heat transfer through radiation is given by Stefan-Boltzmann law as:

$$Q_{radiation} = \varepsilon\sigma(T_{surf})^4 \quad (4)$$

Where ε is the emissivity of the surface being subject to radiant energy, σ is the Stefan-Boltzmann constant at 5.669×10^{-8} W/m^2K^4, T_{surf} is the temperature of the external surface being subject to radiant energy.

3.5.2. Thermophysical modelling of BIPV materials

The BIPV components used for this research were selected from commercially available products in the form of a semi-transparent triple laminated glass with 10% transparency from Onyx Solar (the manufacturer) and a polymer-based roof waterproofing membrane from Axter (the manufacturer). The simulated BIPV glazing consisted of three layers of float glasses and Polyvinyl Butyral (PVB) interlayers, while the central float glass was etched with a-Si PV which had an efficiency of 4.74%. In this case, all the layers were joined together without any air gaps. The roof BIPV membrane consisted of an ETFE polymer with flexible CIGS modules (with an efficiency of 16.6%) encapsulated between an ethylene–vinyl acetate (EVA) sheet on the photoactive side and a Tedlar Polyester Tedlar (TPT) sheet on the backside. The membrane was used along with adhesives and fasteners on top of Plasticised Polyvinyl Chloride (PVC-P) waterproofing sheets and vapour barriers from the same manufacturer for a full waterproofing solution. The simulation model included a thermally insulated and uninsulated version of the composite waterproofing membrane. The physical and thermal properties for each component of both the BIPV glazing and roof membrane were taken from the manufacturer data. Table 2 and Table 3 summarise the respective thermal properties used to model the BIPV glazing and membrane in Ansys Mechanical.

With both BIPVs having transparent and semi-transparent materials on the photoactive sides, the radiative heat fluxes were highly dependent on the transmissivity, reflectivity and absorptivity of each individual material. Table 4 presents the radiation properties of the transparent materials on the photoactive side for both BIPVs. Fig. 4 illustrates the thermal model used for both the BIPV glazing and roof BIPV membrane materials and the energy balance between incident radiative beam, power conversion and heat transfer to surrounding environment.

Furthermore, the thermal radiation properties were used to calculate the boundary conditions for each layer (as per Fig. 4) in Ansys Mechanical. Onyx Solar (the manufacturer) had already been providing the total solar reflection and direct solar transmission factors for the triple laminated glass at 51.3% and 7.4% respectively, which were used to calculate the boundary conditions. Table 5 shows the boundary conditions of each layer based on calculations and assumptions, while the Appendix (attached in this paper) illustrates the meshing and mesh refinement for the FEA simulation in Ansys Mechanical.

3.5.3. Dynamic building performance simulation

The primary output of the dynamic building performance simulation is to analyse how the BIPV materials would impact the thermal loads of the case study building by retrofitting the BIPV glazing and the roof BIPV membrane to the existing building. The DesignBuilder software was used to perform the proposed dynamic building simulation, which adopts the EnergyPlus simulation engine to calculate the cooling load of the building using the following equation [65].

$$\dot{Q}_{load} = \sum_{i=1}^{N_{st}} \dot{Q}_i + \sum_{i=1}^{N_{surfaces}} h_i A_i (T_{si} - T_z) + \sum_{i=1}^{N_{zones}} \dot{m}_i C_p (T_{zi} - T_z) + \dot{m}_{inf} C_p (T_\infty - T_z) \quad (5)$$

Where $\dot{Q}_i$ is the internal load, $h_i A_i (T_{si} - T_z)$ is the convective heat transfer from the zone surfaces, $\dot{m}_i C_p (T_{zi} - T_z)$ is the heat transfer due to interzone air mixing, $\dot{m}_{inf} C_p (T_\infty - T_z)$ is the heat transfer due to infiltration of outside air.

The input parameters for the baseline dynamic thermal model of the case study building are given in Table 6. The building operation loads in terms of lighting power, occupancy and equipment were calculated based on the actual building operations.

The building operating schedules were based on standard office

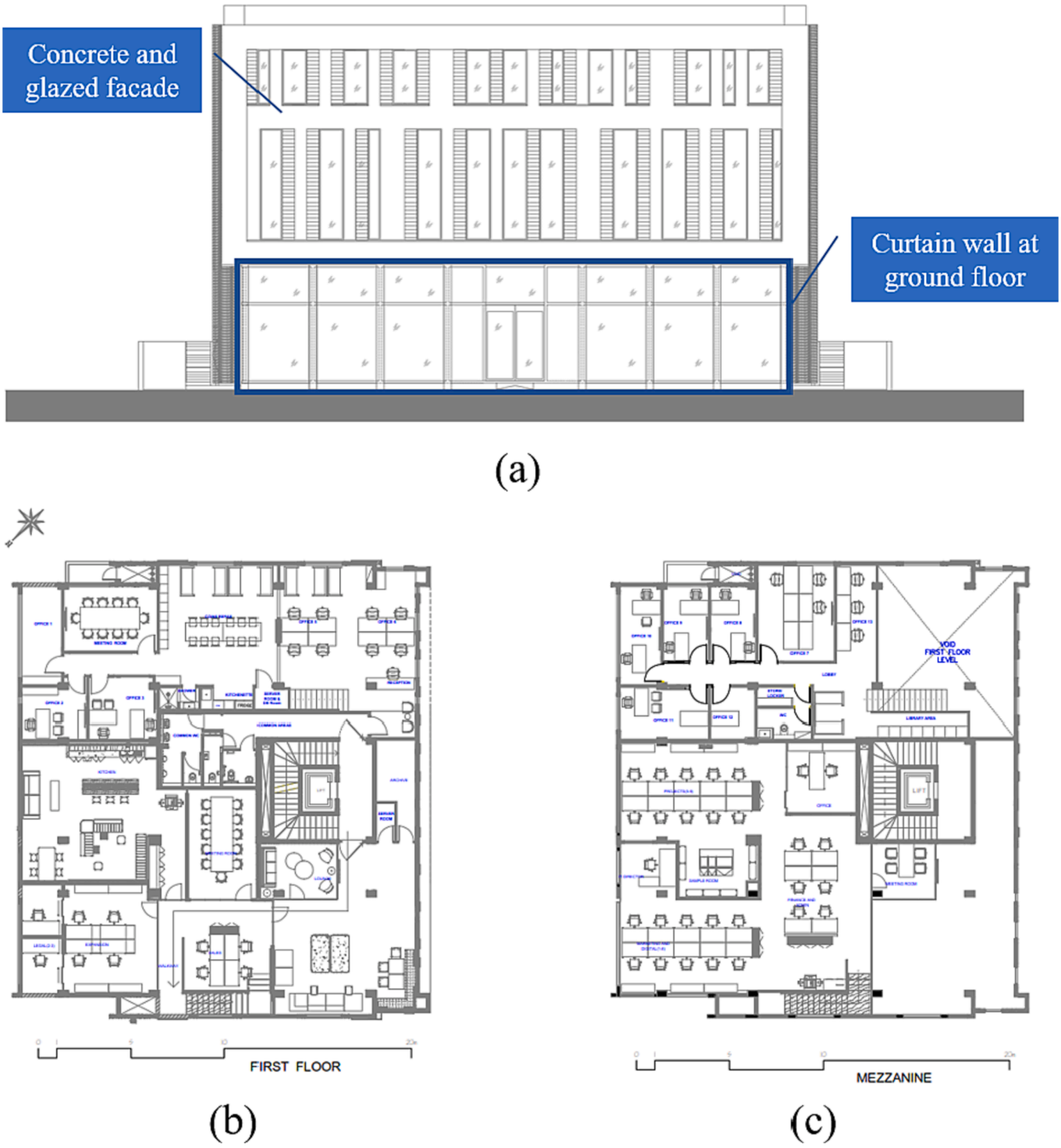

Fig. 3. Architectural drawings of the case study building: (a) south-west façade, (b) typical floor layout, (c) mezzanine layout.

occupancy settings, however, adjusted to match real life scenarios in the course of model calibration. By means of observation and interviews with the building occupants, the schedules were changed to match a low occupancy and remote working scenario due to the aftereffects of the COVID-19 lockdowns in Mauritius. Thus, the schedules for occupancy, cooling, lighting and equipment uses are illustrated in Fig. 5.

The physical modelling with the envelope properties of the baseline building was then performed in DesignBuilder with proper orientations of each wall; while the cooling load simulation of the building was performed for the baseline building first, and then the following retrofits were incorporated and compared to the baseline simulation:

- Option 1 – The south-west façade of the building was substituted with a single BIPV laminate glazing (BIPV curtain wall)
- Option 2 – The roof of the building was substituted with an uninsulated roof BIPV membrane
- Option 3 – The roof of the building was substituted with an insulated roof BIPV membrane

Table 2
Thermal properties of triple laminated BIPV glazing layers.

Material	Thickness (mm)	Thermal conductivity (W/mK)	Specific heat capacity (J/kgK)	Density (kg/m^3)
Low iron glass	6	1.05	750	2500
PVB foil	1.52	0.236	1360	1100
Float glass	3.2	1.05	750	2500
a-Si PV module	0.2	1.8	882	2200

Table 3
Thermal properties of roof BIPV membrane layers.

Material	Thickness (mm)	Thermal conductivity (W/mK)	Specific heat capacity (J/kgK)	Density (kg/m^3)
ETFE	0.3	0.16	2303	1740
EVA	0.5	0.311	2090	960
CIGS PV module	0.33	3.7	300	5770
TPT	0.3	0.15	1250	1200
Butyl adhesive	1	0.24	1400	1200
Nylon fastener	2.35	0.25	1600	1150
PVC-P membrane	1.5	0.17	900	1390
Polyisocyanurate (PIR) insulation	25	0.025	1500	33.6
Vapour barrier	1.2	0.38	1700	1460

Table 4
Radiation properties of BIPV transparent layers.

Material	Transmissivity	Reflectivity	Absorptivity	Emissivity
ETFE	0.926	0.065	0.009	0.94
EVA	0.900	0.020	0.08	–
Low iron glass	0.84	0.08	0.08	–
PVB	0.82	0.07	0.11	–
Float glass	0.88	0.08	0.04	–

- Option 4 – The south-west façade of the building was partially substituted with a naturally ventilated double-skin façade incorporating a single BIPV laminate glazing in the front layer for the first and second floors, while the ground floor façade was kept as the BIPV curtain wall only

The baseline and retrofits modelled in DesignBuilder are shown in Fig. 6 and Fig. 7, respectively.

3.5.4. Building energy modelling

The building energy modelling, in terms of energy usage and PV electricity generation of each of the proposed BIPV typologies, was performed in DesignBuilder to assess the impact of the BIPVs on the building's energy end-use. For the whole building energy assessment,

Table 5
Thermal boundary conditions for FEA simulation.

Boundary condition parameter	Value	Source
Radiative heat fluxes		
Triple laminated BIPV glazing (a-Si)		
Q_{solar}	1027.948 W/m^2	Based on Section 3.5.1 and Table 4
$Q_{reflect}$	527.337 W/m^2	Based on Section 3.5.1 and Table 4
Q_{glass}	82.236 W/m^2	Based on Section 3.5.1 and Table 4
Q_{PVB}	94.982 W/m^2	Based on Section 3.5.1 and Table 4
Q_{float}	28.322 W/m^2	Based on Section 3.5.1 and Table 4
Q_{elec}	48.725 W/m^2	Based on Section 3.5.1 and Table 4
$Q_{D\text{-}Tr}$	76.068 W/m^2	Based on Section 3.5.1 and Table 4
Q_{PV}	170.278 W/m^2	Based on Section 3.5.1 and Table 4
Roof BIPV membrane (CIGS)		
Q_{solar}	959.333 W/m^2	Based on Section 3.5.1 and Table 4
$Q_{reflect}$	80.124 W/m^2	Based on Section 3.5.1 and Table 4
Q_{ETFE}	8.634 W/m^2	Based on Section 3.5.1 and Table 4
Q_{EVA}	71.067 W/m^2	Based on Section 3.5.1 and Table 4
Q_{elec}	159.249 W/m^2	Based on Section 3.5.1 and Table 4
Q_{PV}	640.259 W/m^2	Based on Section 3.5.1 and Table 4
Convective heat transfer coefficient		
h_{ext}	13 W/m^{2}K	BS EN ISO 6946:2017 [64]
$h_{int\text{-}v}$	2.5 W/m^{2}K	BS EN ISO 6946:2017 [64]
$h_{int\text{-}h}$	0.7 W/m^{2}K	BS EN ISO 6946:2017 [64]
Air temperatures		
T_{ext}	32.9 °C	Simulation condition
T_{int}	25 °C	Simulation condition

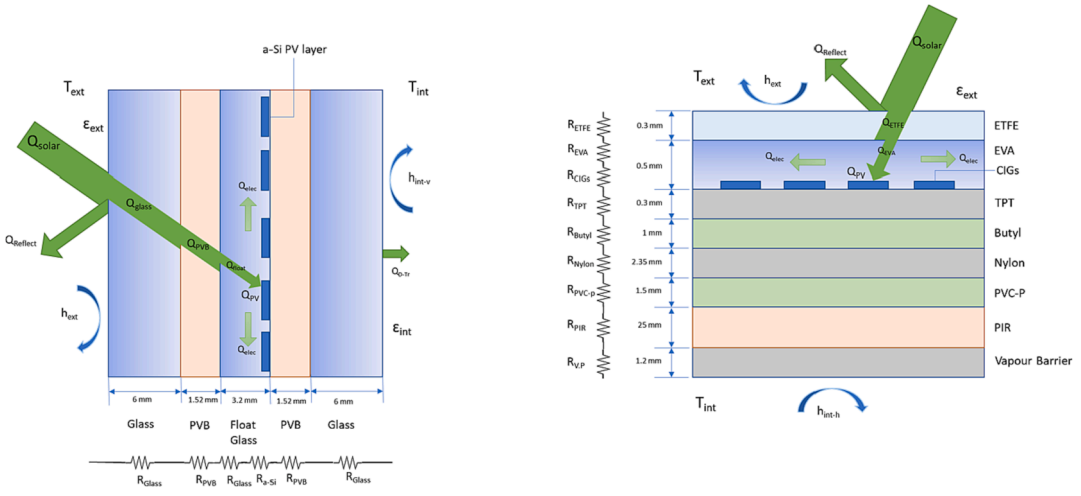

Fig. 4. Thermal energy balance schematics: BIPV glazing (left), roof BIPV membrane (right).

Table 6
Input parameters for dynamic simulation of the building.

Input parameter	Value
U-value of the external wall	1.916 W/m^{2}K
U-value of the internal wall	1.501 W/m^{2}K
U-value of the roof	2.204 W/m^{2}K
U-value of the intermediate floor	2.036 W/m^{2}K
U-value of the external window	1.772 W/m^{2}K
Air permeability	0.7 ACH
Cooling set point	24 °C
Occupancy density (ground floor)	0.082 person/m^2
Occupancy density (first floor)	0.043 person/m^2
Occupancy density (second floor)	0.013 person/m^2
Heat gain from occupant	150 W/person
Lighting power density (ground floor)	3.9 W/m^2
Lighting power density (ground floor mezzanine)	5.1 W/m^2
Lighting power density (first floor)	4.7 W/m^2
Lighting power density (first floor mezzanine)	6.1 W/m^2
Lighting power density (second floor)	5.1 W/m^2
Equipment power density (offices)	2.3 W/m^2
Equipment power density (common areas)	2.7 W/m^2

the services to each zone were simulated to imitate a full operation scenario of the case study building to investigate the energy impact. The inputs for lighting and equipment uses for the building are shown in Table 6. To meet the cooling load calculated in **Eq. (5)**, the HVAC systems consisting of a DX split system were modelled based on the **Eq. (6)** used in association with the DesignBuilder simulation [65].

$$\dot{Q}_{sys} = \dot{m}_{sys} C_p \left(T_{sup} - T_z\right) \tag{6}$$

Where $\dot{m}_{sys}$ is the mass flow rate provided by the DX split system, C_p is the zone air specific heat, T_{sup} is the supply air temperature, T_z is the zone mean air temperature.

The BIPV construction material feature of DesignBuilder was used to simulate the PV electricity generation following the equivalent one-diode model, which was calculated by using the following equation [65]:

$$I = I_L - I_o \left[exp\left(\frac{q}{\gamma k T_{PV}}(V + IR_s)\right) - 1 \right] \tag{7}$$

Where I is the current in the one-diode equivalent circuit, I_L is the PV module photocurrent, I_o is the diode reverse saturation current, q is the elementary charge at 1.602×10^{-19}C, γ is the empirical PV curve-fitting parameter, k is the Boltzmann's constant at 1.381×10^{-23} J/K, T_{PV} is the PV module temperature, V is the voltage in the one-diode equivalent circuit, R_s is the PV module series resistance.

Fundamentally, the generated PV electrical power is given by "$P = IV$", where it is required to obtain the current I and voltage V through three known I-V points. The three points are the short circuit current (I_{sc}), the open-circuit voltage (V_{oc}) and the maximum power output (P_{mpp}), while the corresponding temperature coefficients are also crucial. Table 7 shows the inputs for the BIPV module obtained from manufacturer documentations, which were used as the BIPV module inputs in the DesignBuilder model. In this study, 508 m^2 of roof space and 342 m^2 of façade space were used for the roof and façade BIPV retrofits, respectively. Specifically, the roof retrofit consisted of 146 × 500 W and 17 × 200 W CIGS roof membrane modules, while the façade retrofit consisted of 209 × 62 W and 19 × 32 W semi-transparent a-Si modules. The PV electricity generation was allowed to run for the whole year including weekends to assess its complete capability.

4. Model calibration

4.1. Energy model calibration

Building energy consumption, as the core research output reflecting thermal and energy performance of the case study building, was selected for calibration to match real data of the building to gauge the model's suitability as an evaluation tool for the BIPV retrofits. The calibrated model had several office spaces switched off to match real life operations during the year 2021 for which annual energy usages were available. Specifically, a baseline model of building energy consumption was first calibrated using actual metered energy consumption from the utility provider. Since it was the second year of operation of the building, several offices were still unoccupied on the second floor, east wing of first floor and west wing of ground floor. Thus, the building services systems to those offices were switched off for the baseline calibration.

The ASHRAE 14 [66] monthly acceptance indices – Mean Bias Error (MBE) and Cumulative Variation of Root Mean Squared Error (CVRMSE) – were used to evaluate the energy model calibration. The acceptable criteria for the MBE and CVRMSE are within ± 5% and less than 15%, respectively, and both are calculated as follows:

$$MBE = \frac{\sum_{i=1}^{N_P}(M_i - S_i)}{\sum_{i=1}^{N_P} M_i} \tag{8}$$

$$\overline{M_P} = \frac{\sum_{i=1}^{N_P} M_i}{N_P} \tag{9}$$

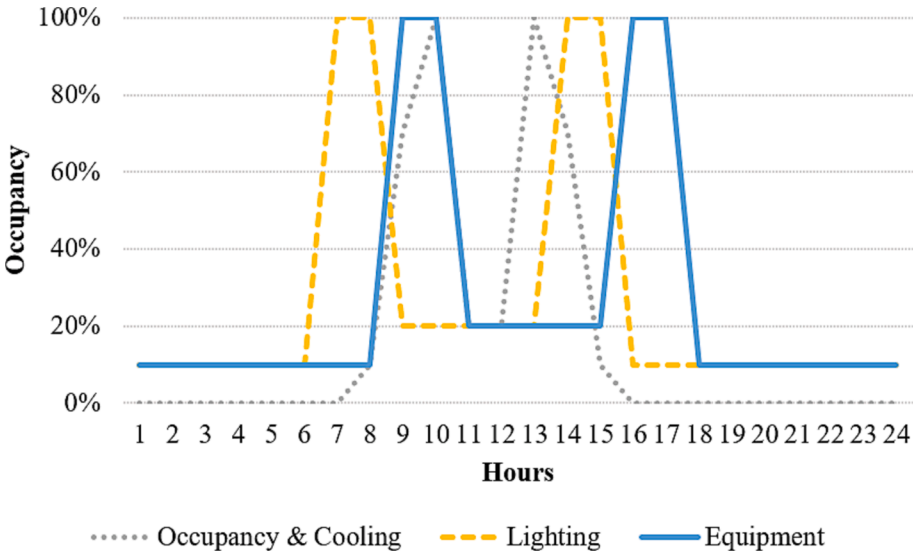

Fig. 5. Operating schedules for the case study building.

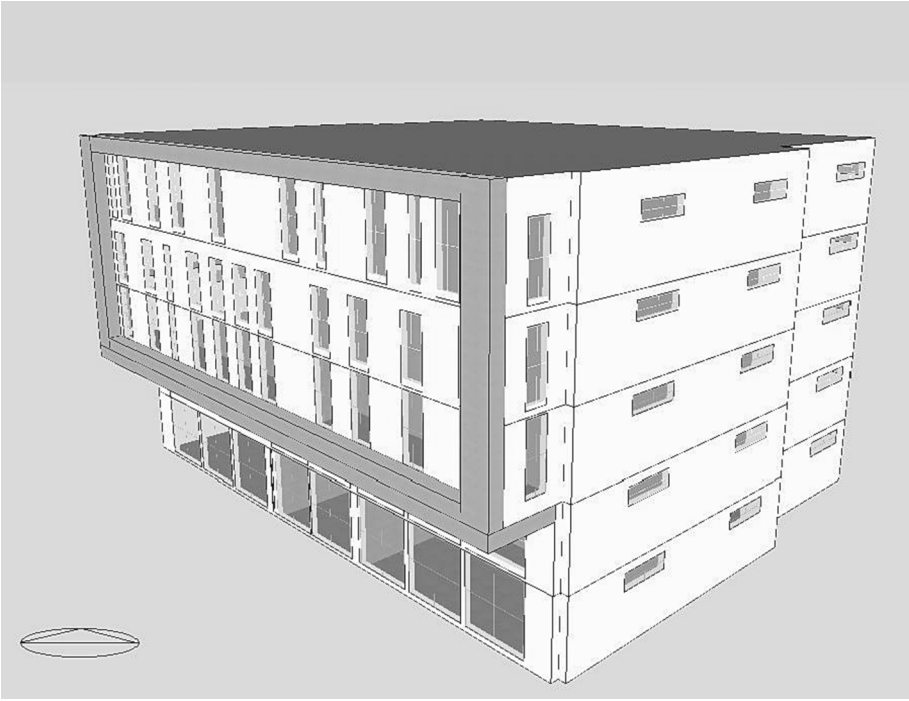

Fig. 6. 3D view of the baseline model.

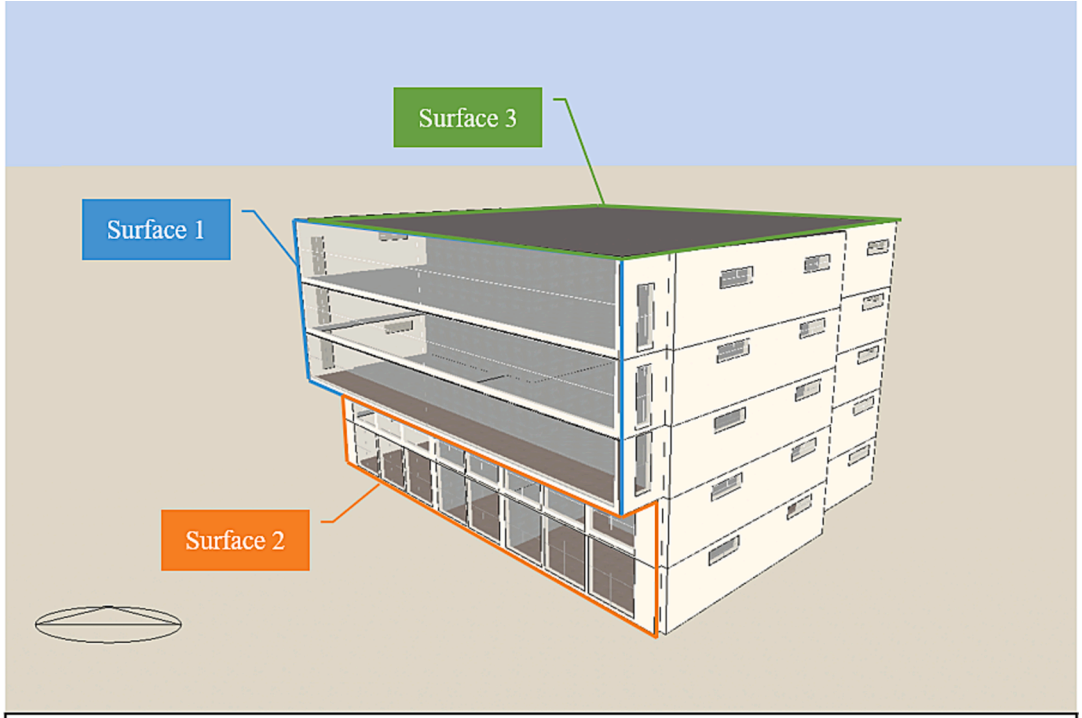

	Surface 1	Surface 2	Surface 3
Option 1	BIPV curtain wall	BIPV curtain wall	Baseline setting
Option 2	Baseline setting	Baseline setting	Uninsulated roof BIPV membrane
Option 3	Baseline setting	Baseline setting	Insulated roof BIPV membrane
Option 4	BIPV-DSF	BIPV curtain wall	Baseline setting

Fig. 7. 3D view of the BIPV retrofit options.

Table 7
I-V characteristics of the BIPV modules for the retrofits.

Parameter	Semi-transparent a-Si BIPV module		CIGS roof membrane BIPV module	
	62 W	32 W	500 W	200 W
Area (m^2)	1.39	0.71	2.33	0.94
Rated power (W)	72.32	32	500	200
Short circuit current, I_{sc} (A)	1.15	1.15	9.07	8.82
Current at max output, I_{mpp} (A)	1.04	0.93	8.03	8.27
Temperature coefficient of I_{sc} (A/°C)	0.000104	0.000104	0.00073	0.00071
Open circuit voltage, V_{oc} (V)	94	50	77.2	29.2
Voltage at max output, V_{mpp} (V)	70.5	34	62.4	24.2
Temperature coefficient of V_{oc} (A/°C)	−0.26	−0.14	−0.216	−0.082
NOCT ambient temperature (°C)	20	20	20	20
NOCT cell temperature (°C)	45	45	48	48

$$CVRMSE = \frac{\sqrt{\sum_{i=1}^{N_P}\left(\frac{(M_i - S_i)^2}{N_P}\right)}}{\overline{M_P}} \quad (10)$$

Where M_i and S_i are the respective measured and simulated data at instance "i", P is the calculation time interval; N_P is the number of values at interval P, $\overline{M_P}$ is the average of the measured data.

The model calibration process, as illustrated in Fig. 8, was used to get a calibrated energy model that would meet the ASHRAE 14 acceptable criteria [66]. In summary, major parameters affecting the accuracy of the simulation results including weather data, physical properties of the building envelope and BIPV modules, internal gains and other operational settings were fine-tuned to match the measured electrical utility data with an acceptable level of accuracy. Since the HVAC system was a DX split system with the indoor temperatures defined by the occupants, it was assumed that the setpoints varied considerably over the year. To tackle this issue two setpoints were used for the baseline energy model calibration, namely 25 °C during summer months when temperatures were already high and 22 °C during winter months when outdoor temperatures were relatively low.

Fig. 9 shows the final iteration of the simulated energy consumption and the utility energy measurements on a monthly basis for a whole year along with the percentage deviation (based on the CVRMSE) between

Table 8
Results of acceptance indices for energy model calibration.

Indices	Summer (Oct – Mar)	Winter (Apr – Sep)	Annual (Jan – Dec)	Acceptance criteria	Met acceptance criteria?
MBE	−3%	2%	−0.3%	Within ± 5%	Yes
CVRMSE	6%	5%	1.1%	≤ 15%	Yes

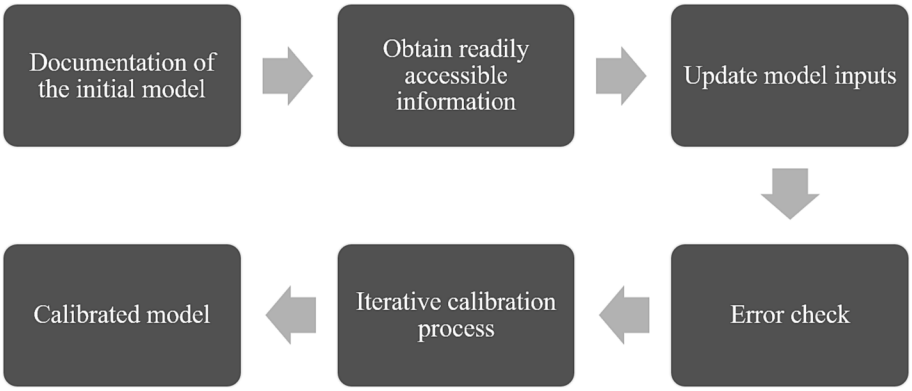

Fig. 8. Process of model calibration method [67].

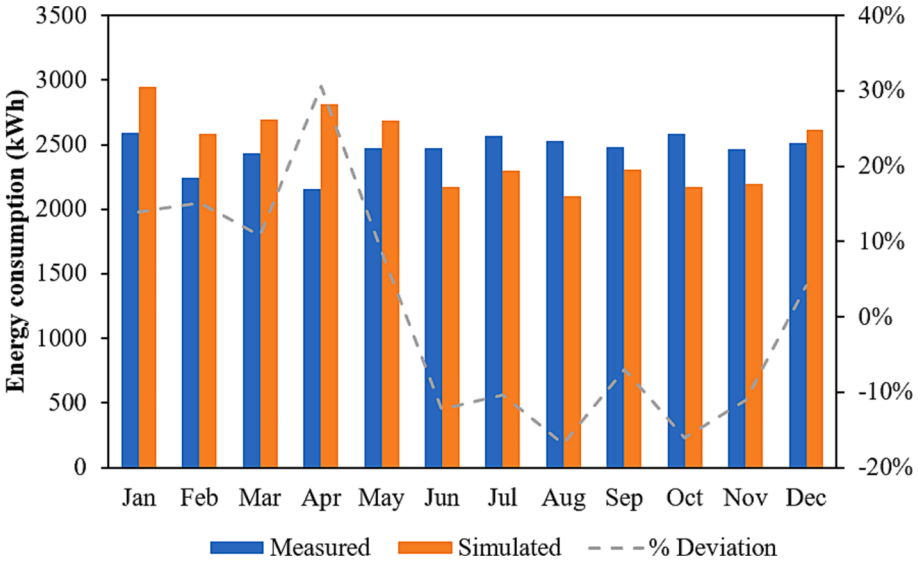

Fig. 9. Monthly simulated energy consumption versus measured energy consumption.

Table 9
Results of finite element heat transfer model calibration.

Scenario	RRMSE	Excellent accuracy	Good accuracy	Fair accuracy	Poor accuracy
BIPV glazing	0.014%	RRMSE < 10%	10% ≤ RRMSE ≤ 20%	20% ≤ RRMSE ≤ 30%	RRMSE > 30%
Roof BIPV membrane	0.023%				

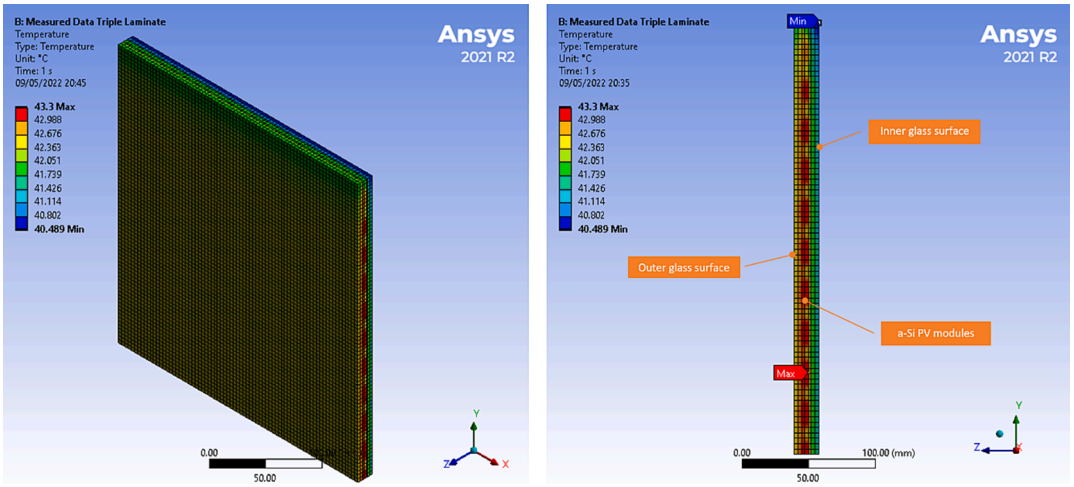

Fig. 10. Isometric view of temperature distribution on the laminated BIPV glazing (left), side view of maximum and minimum temperatures on the laminated BIPV glazing (right).

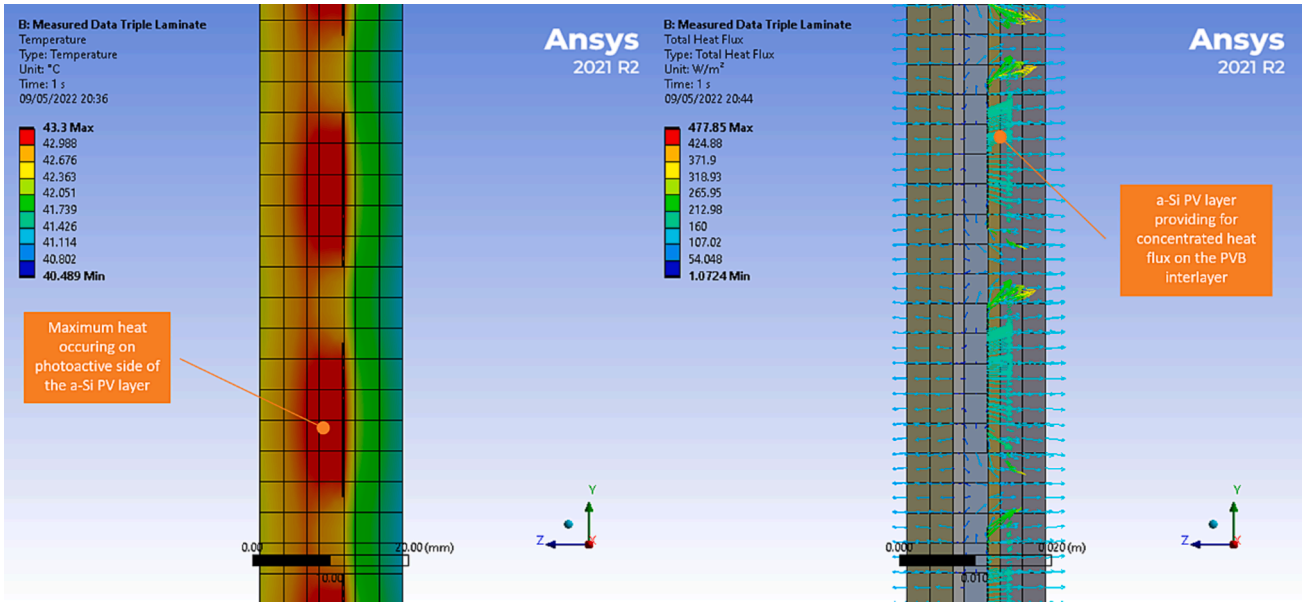

Fig. 11. Close-up cross section views of temperature and heat distributions on the laminated BIPV glazing.

both energy results. It can be seen that most of the corresponding simulated and measured results matched well to each other; the highest deviation occurred in April, while the remaining months stayed within the 15% threshold of the CVRMSE.

Since two temperature setpoints being used in different seasons of the year, the calibration was further divided into a summer period, a winter period and an annual period. As can be seen in Table 8, all the monthly MBE and CVRMSE indices were well within the set limits for all the periods, while the annual indices showing the closest fit to measured data. Thus, the model was deemed calibrated.

4.2. *Finite element heat transfer model calibration*

In addition to the building energy modelling, the finite element heat transfer modelling was another crucial part of the study, which was also calibrated (as per the calibration process shown in Fig. 8) while using a different evaluation method. To calibrate the results from the FEA, the PV cell temperature (T_c) was selected as the calibration parameter. Fundamentally, PV cell temperature is determined through the Nominal Operating Cell Temperature (NOCT) model [68] as per **Eq. (11)**:

$$T_c = T_a + (NOCT - 20) \bullet \frac{I_s}{800} \tag{11}$$

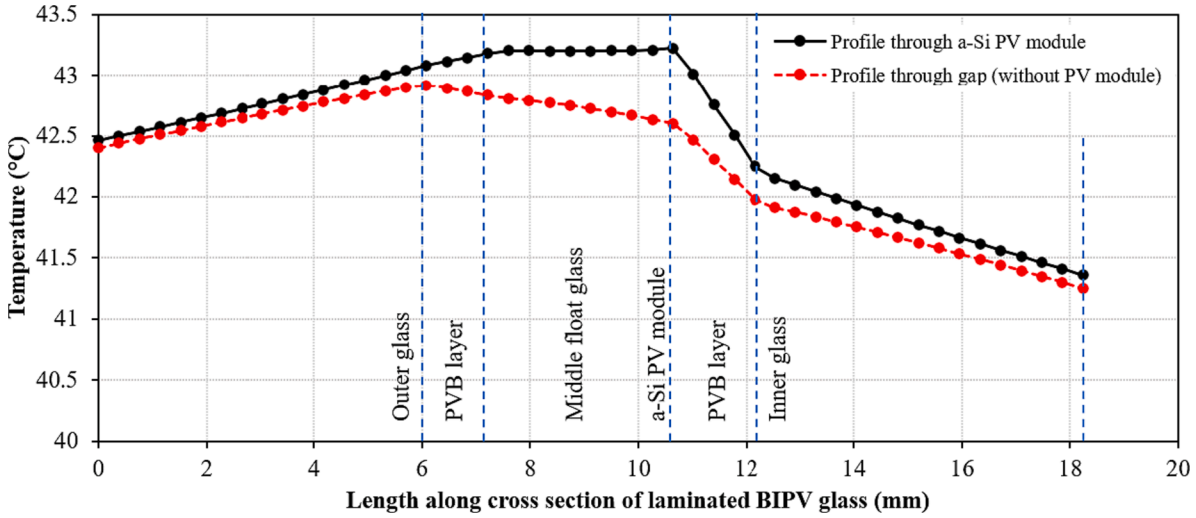

Fig. 12. Temperature profile along cross section of laminated BIPV glazing.

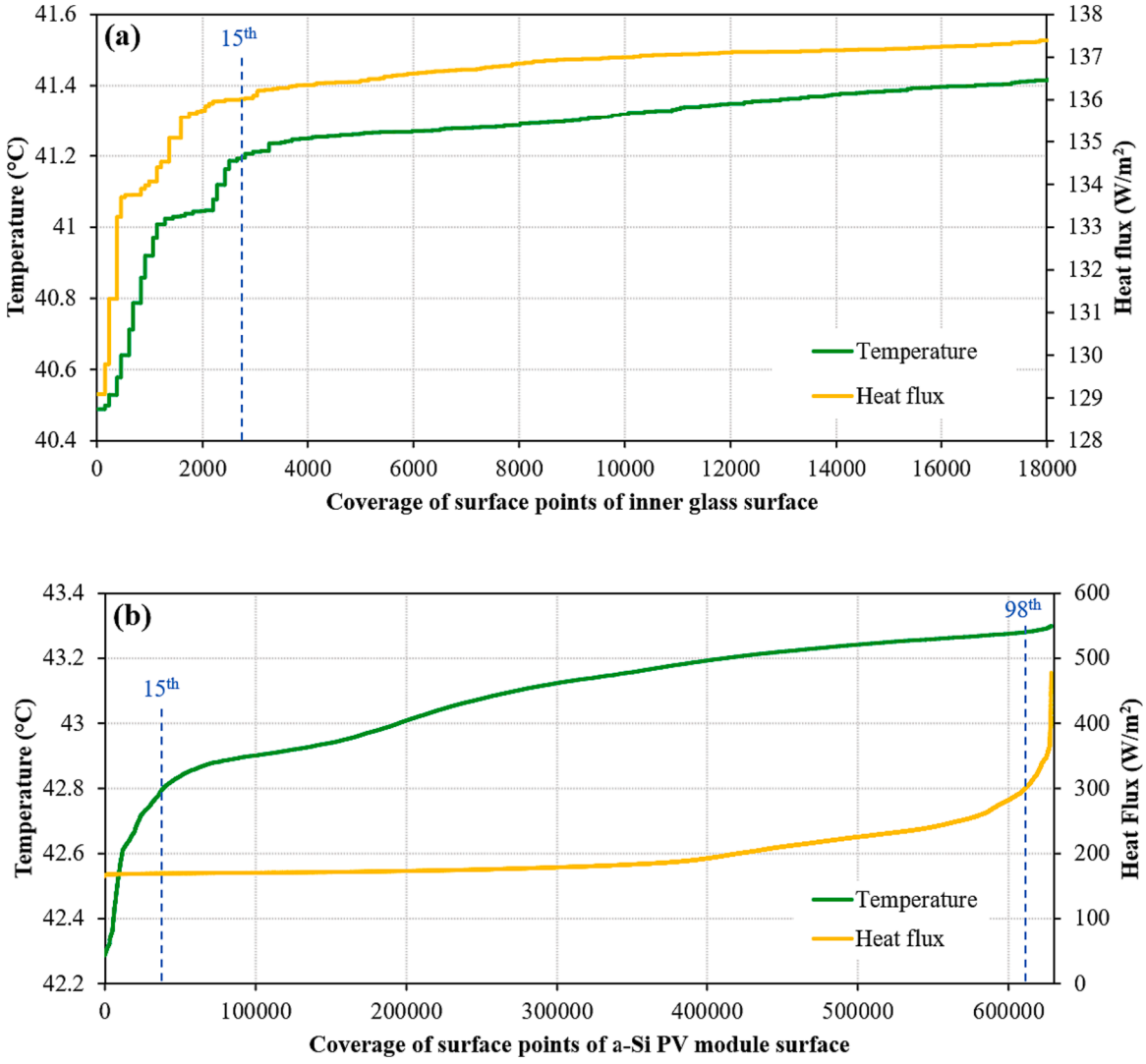

Fig. 13. Cumulative frequency heat metrics for: (a) inner glazing surface, (b) a-Si PV module surface.

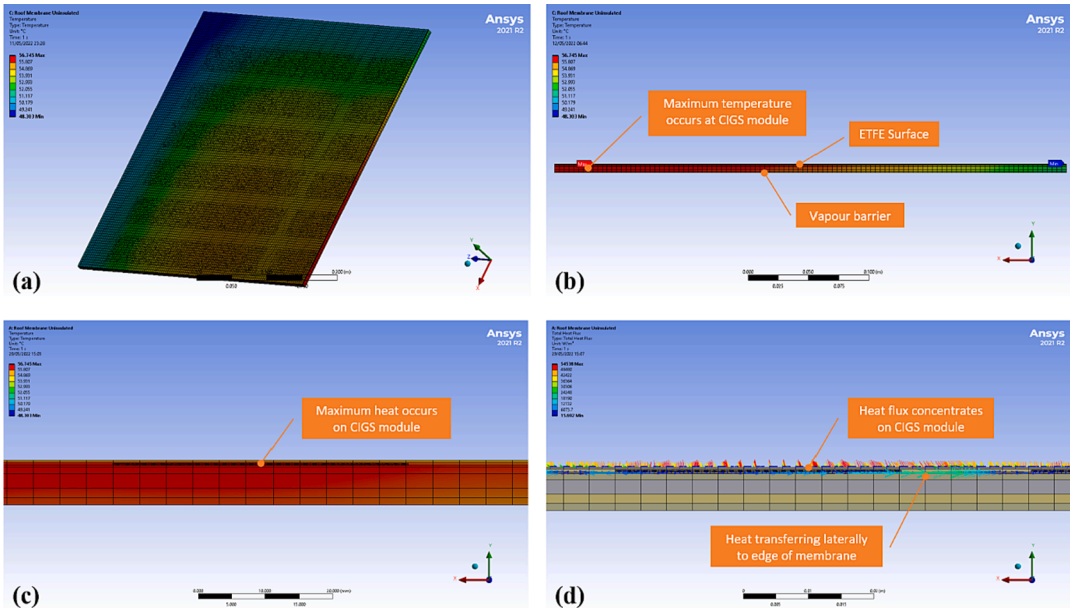

Fig. 14. Temperature and heat distributions on uninsulated roof BIPV membrane: (a) isometric view of temperature distribution, (b) side view of maximum and minimum temperatures, (c) close-up cross section view of temperature distribution, (d) close-up cross section view of heat distribution.

Where T_a is the ambient air temperature, I_s is the incident solar radiation on the cell surface.

Using the data given in Table 5 and Table 7, the PV cell temperatures for both the a-Si BIPV glazing and the CIGS roof BIPV membrane were calculated, where only the uninsulated membrane scenario was considered for the roof BIPV modelling calibration due to the availability of the data. The PV cell temperatures obtained through the ANSYS simulation were then compared to the calculated PV cell temperatures using the measure of Relative Root Mean Square Error (RRMSE), which is calculated as follows [69]:

$$RRMSE = \sqrt{\frac{\frac{1}{n}\sum_{i=1}^{n}(x_i - y_i)^2}{\sum_{i=1}^{n}(y_i)^2}} \tag{12}$$

Where y_i is the simulated value, x_i is the calculated value, n is the total number of data samples (that is, the total number of the PV cell temperature samples).

In summary, the RRMSE values for both scenarios of BIPV glazing and roof BIPV membrane along with the accuracy bands [69] are tabulated in Table 9. As can be seen, both scenarios of the FEA simulation were within the excellent accuracy, thus the models were deemed calibrated.

5. Results and discussion

5.1. Finite element heat transfer analysis

This section evaluates the capability of the finite element heat transfer analysis to predict the heat transfer characteristics of the triple laminated BIPV glazing and both insulated and uninsulated versions of the roof BIPV membranes.

5.1.1. Heat transfer through triple laminated BIPV glazing

The results from the finite element heat transfer analysis for the BIPV glazing are illustrated in Fig. 10, where the temperature distribution over the whole test piece is shown. The results show that the a-Si PV module in the interlayer had the highest temperatures at 43.3 °C, while the lowest temperature occurred at the edge of the glazing which was enclosed in a frame at 40.489 °C. The distribution clearly shows that the a-Si PV module was heating up from the effect of incident radiation and emitting the heat to its surroundings to provoke the high temperatures on the surface. Fig. 11 presents a close-up of the cross section, which shows heat concentration occurring on the photoactive side of the a-Si PV module. In this case, the resultant heat flux was predominantly occurring from the PV module to the inner surface of the glazing with the highest heat fluxes happening through the gaps between the strips on the edges of the PV module.

To further verify that whether the resultant heat was dominated by the PV module, a temperature profile along the cross section of the laminated BIPV glazing is presented in Fig. 12. It is found that the highest temperature occurred on the a-Si PV module itself, while if a gap substitutes the PV module layer the highest temperature occurred at the outer PVB layer. This indicates that the PV module was absorbing a considerable amount of radiative heat, which was then being emitted to its surrounding. However, both trends being dropped similarly after the entire glazing to reach the average inner glazing temperature of 41.4 °C.

Furthermore, temperature variations on the laminated BIPV glazing surfaces were evaluated for a better assessment of the impact of the BIPV glazing on building cooling loads. Fig. 13 shows the cumulative frequency distribution of the temperature and resultant heat flux on both inner glass surface and a-Si module of the laminated glazing. It can be observed that the heat flux had a close correlation with the temperature of the nodes happening on the inner glass surface. The curves show that the 15th percentile marker amounting to 41.2 °C (temperature) and 136 W/m^2 (heat flux), which means that for 85% of the inner glass surface area the temperature varied between 41.2 °C and 41.4 °C, while the heat flux remained between 136 W/m^2 and 137.4 W/m^2. According to local thermal discomfort definition given by ASHRAE 55 [70], these resultant temperatures varying on the inner glass surface (as a "Warm Wall") can significantly lead to local thermal discomfort. Thus, a considerable cooling energy certainly will be consumed to maintain thermal comfort in the building, which is discussed in the Section 5.2 of this paper. For the a-Si PV module surface, both curves had opposing profiles below the 15th percentile and above the 98th percentile, however, the discrepancy accounted for an overall 17% of the surface only, while for 83% of the nodes both heat metrics stayed relatively constant between 42.8 °C and 43.3 °C for the temperature and 170 W/m^2 and 300 W/m^2 for the heat flux. Apparently, the higher resultant temperatures of PV module surface, to a large extent, led to the "Warm Wall" affecting thermal performance of the entire laminated BIPV glazing.

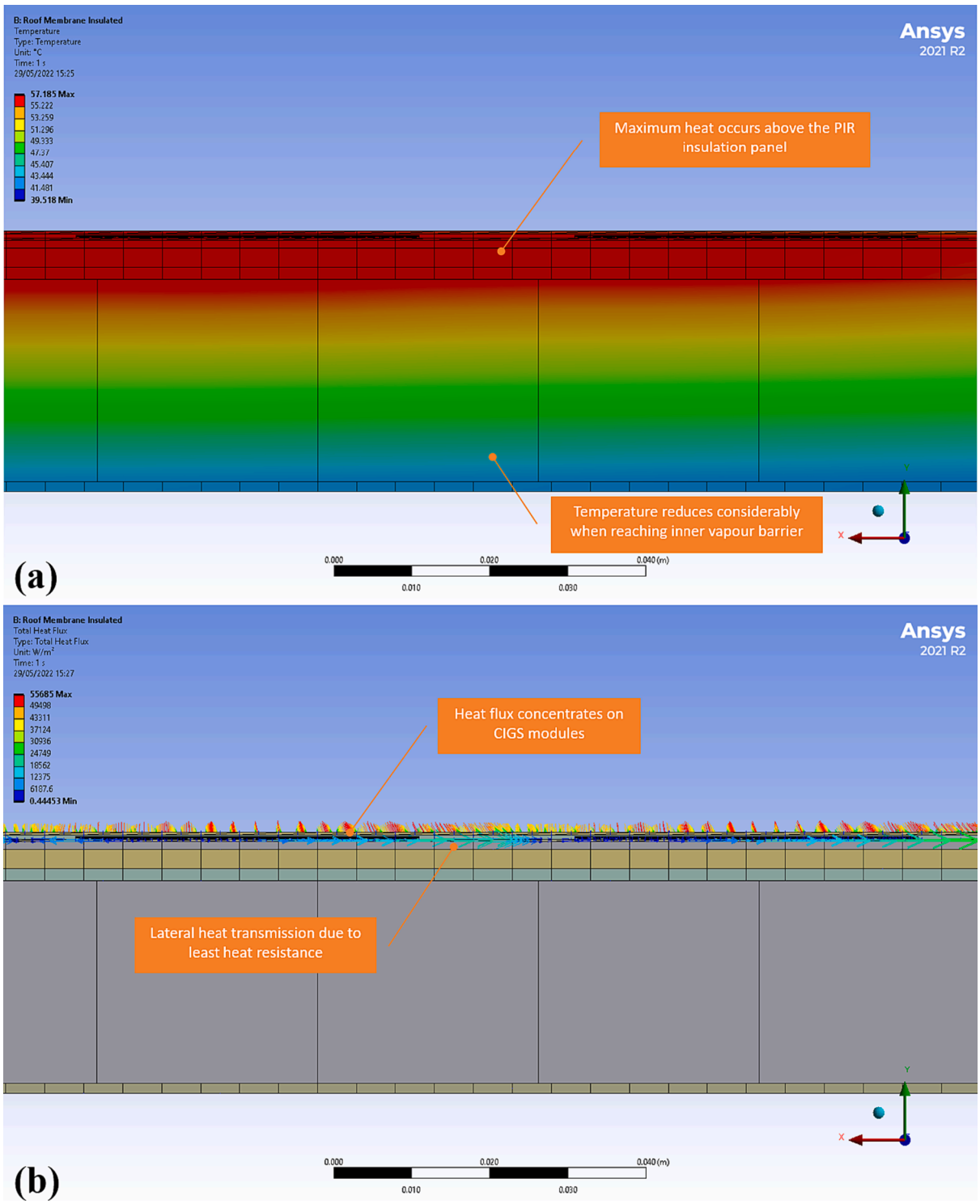

Fig. 15. Close-up cross section view of temperature and heat distributions on insulated roof BIPV membrane.

5.1.2. Heat transfer through roof BIPV membrane

Fig. 14 provides the results of the finite element heat transfer analysis for the uninsulated roof BIPV membrane, where the temperature distributions of the test piece are shown. Similar to the laminated BIPV glazing, the uninsulated roof BIPV membrane had the highest temperature on the CIGS PV module layer at 56.745 °C and the lowest temperature along the edges of the membrane which were the furthest from the heated PV modules at 48.303 °C, while average inner surface temperature at the vapour barrier was about 53.78 °C. As shown by the close-up cross sections of the uninsulated membrane in Fig. 14, the maximum heat occurred under the CIGS PV module but, the heat flux directed towards the edges of the component rather than through the other membrane layers. Fundamentally, the PV modules were processing maximum heat by absorbing and emitting it to the surrounding layers; however, in comparison with the BIPV glazing which is transparent and transmits incident radiation, the heat transfer of the roof BIPV membrane was reduced considerably due to the opacity of the TPT back layer. In this case, heat transfer occurred mostly through conduction underneath the TPT layer and onto the waterproofing layers.

Fig. 15 shows the cross section of the insulated roof BIPV membrane.

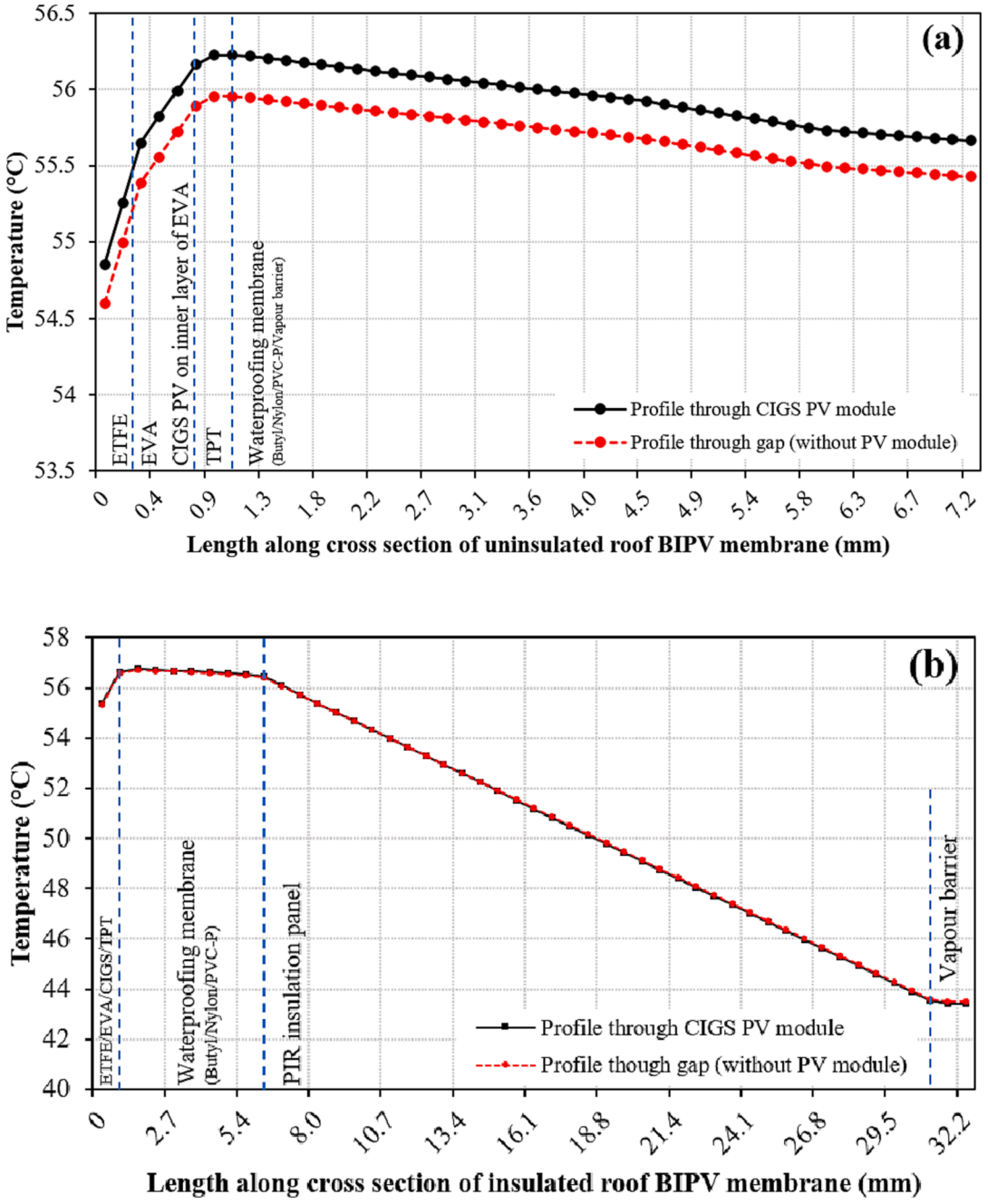

Fig. 16. Temperature profile along cross section of: (a) uninsulated roof BIPV membrane, (b) insulated roof BIPV membrane.

The temperature of the membrane was seen to reduce considerably from 57.185 °C to 39.518 °C due to the inclusion of the PIR insulation panel, and the average inner surface temperature at the vapour barrier was 42.3 °C. Basically, most of the heat occurred and transferred on the topmost layers of the membrane (above the insulation panel). Similar to the uninsulated version, the heat flux was diffusing sideways to the edges above the waterproofing layers.

Fig. 16 shows both temperature profiles along the cross section of the uninsulated and insulated roof BIPV membranes, through both the CIGS PV module and the gap (without the CIGS PV module) within the membranes. For the uninsulated scenario, even though the temperatures through the CIGS module was slightly higher, both profiles followed similar trends peaking at the PV module/gap layer and then gradually decreased to inner surface temperature. The average difference between the two trends amounted to only about 0.253 °C. However, the inner surface temperature was at an average of 55.54 °C, which was higher than the initial photoactive side of the uninsulated roof BIPV membrane; this means thermal resistances of the under layers were too low to resist the amount of heat transmitted from the PV modules (GIGS), and consequently heat transfer to the adjoining construction materials during a normal installation would be high. For the insulated scenario, it can be seen that both profiles had very similar trends peaking at the PV modules (CIGS) and decreasing towards the inner surface temperature. However, unlike the uninsulated membrane, the insulated one with PIR panel had a significantly lower inner surface temperature at an average of 43.45 °C with an effective temperature drop around 12 °C noted over the cross section. This demonstrates that the advantage of the PIR insulation panel in controlling heat transmission through the roof BIPV membrane.

Fig. 17 presents the cumulative temperature and heat flux

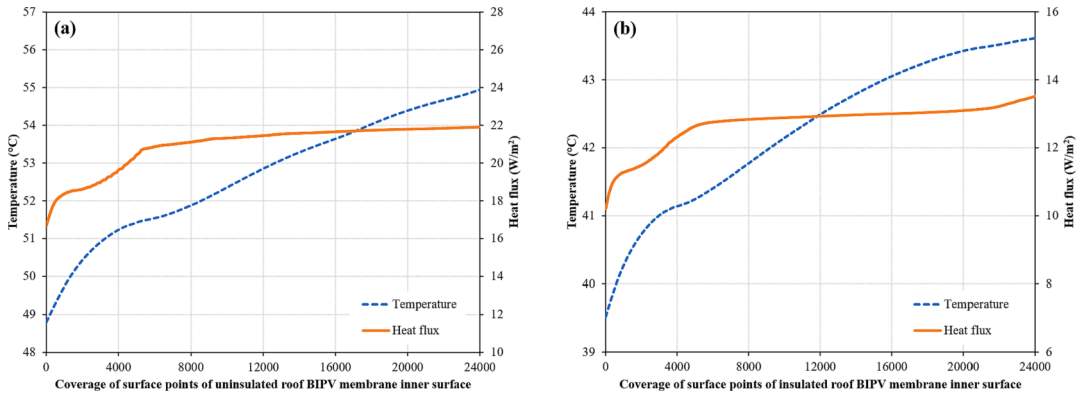

Fig. 17. Cumulative thermal metrics for roof BIPV membrane inner surfaces: (a) uninsulated, (b) insulated.

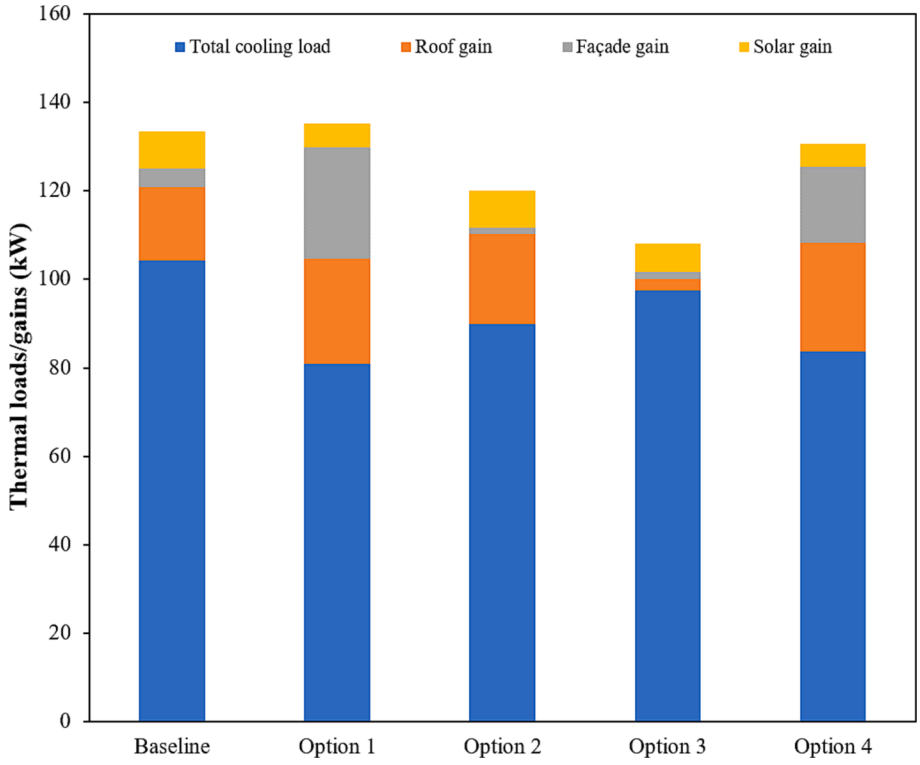

Fig. 18. Peak thermal loads/gains for different design options.

distributions of the inner surfaces for both the insulated and uninsulated roof BIPV (CIGS) membranes. Both distributions show a relatively steady heat flux, of which 22 W/m^2 for the uninsulated scenario and 13 W/m^2 for the insulated scenario; while the temperature distributions over the simulated nodes of the inner surfaces were within the range of 49–55 °C (6 °C in difference) and 39.5–43.5 °C (4 °C in difference), respectively, for the uninsulated and insulated scenarios. This has further demonstrated that the PIR insulation panel was active in cooling the roof BIPV membrane surface down, as well as restraining the significant heat transmission along the surface.

5.2. *Dynamic building performance analysis*

The building's peak cooling load results for each of the BIPV retrofit options from the dynamic building simulations are shown in Fig. 18. The design options' cooling loads were compared to that of the baseline, and the cooling loads were referred to the corresponding heat gains from the façade elements, the roof, and the direct solar radiations, as well as the internal gain (which was not presented as this was not a design variable). With the baseline peaking at 133 kW, Option 1 with the BIPV curtain wall had a slight increase of about 1 % to reach 135 kW. In comparison, Options 2 and 3 with the roof BIPV membranes had a most effective reduction with 8 % at 119.85 kW for the uninsulated roof membrane and 15 % at 112.02 kW for the insulated roof membrane, while Option 4 with the BIPV-DSF had a slight reduction of 2 % to reach 130 kW. This clearly shows that the roof BIPV membranes had the most impact in terms of thermal transmission and overall heat balance; while the poorer thermal performance of the BIPV façades was likely due to the nature of the BIPV glazing, as higher thermal mass in the form of solid walls were largely substituted by BIPV glazing with a relatively higher heat transfer coefficient and SHGC.

The hourly variations of building heat balance for each BIPV retrofit option are presented in Fig. 19. The heat gains are shown in the positive domain of the X-axis, while the heat losses in the form of cooling energy or heat transferred out of the zones are shown in the negative domain. The hourly data was plotted against the outdoor dry bulb temperature

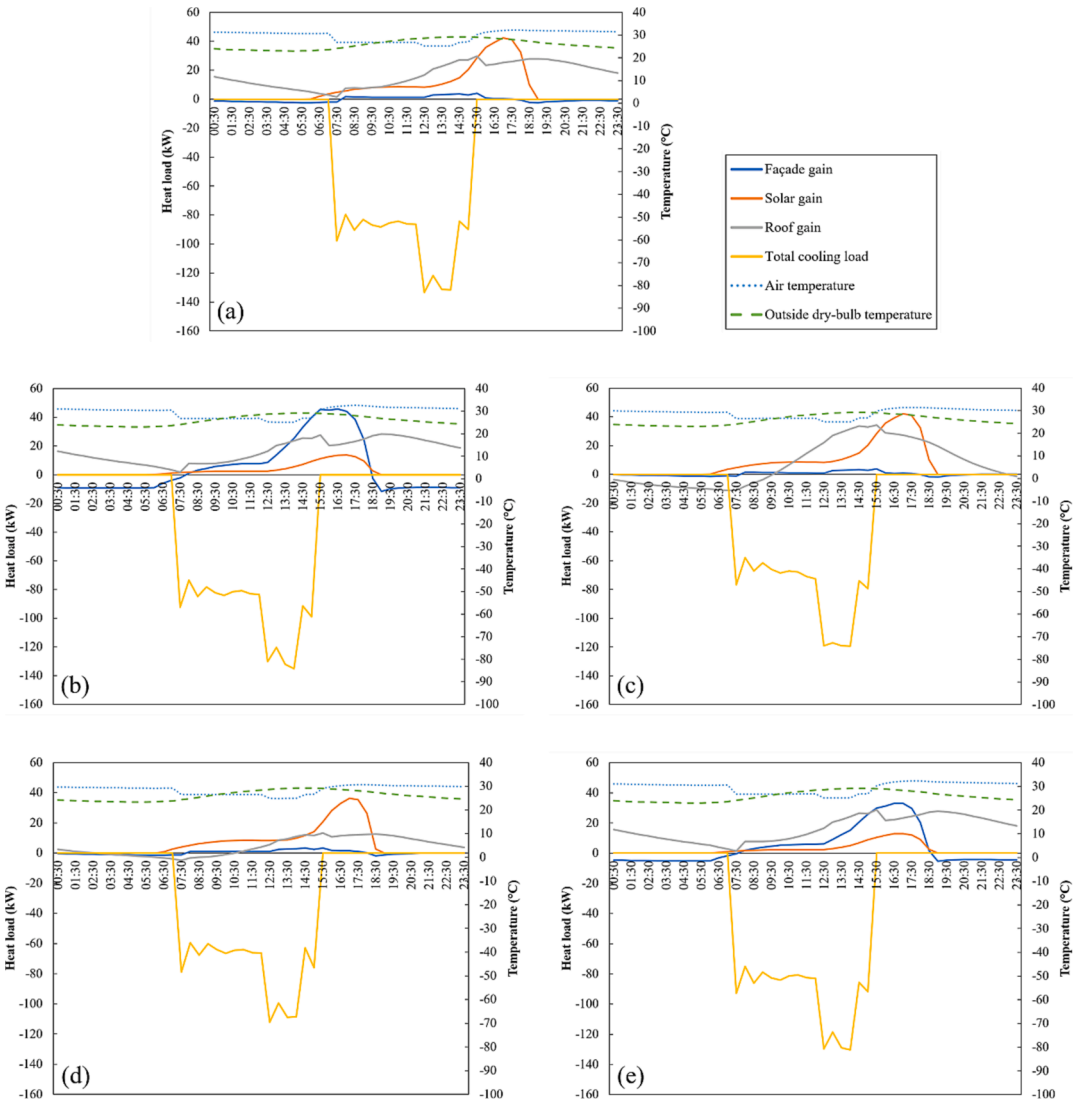

Fig. 19. Hourly heat balance for different design options: (a) baseline model, (b) Option 1 – BIPV curtain wall, (c) Option 2 – uninsulated roof BIPV membrane, (d) Option 3 – insulated roof BIPV membrane, (e) Option 4 – BIPV-DSF.

and indoor average air temperature resulting from the heat balance and cooling process. In the baseline case, all the heat gains remained in the positive domain with solar heat transmissions from glazing and conductive heat gains from roof had the biggest impacts on the total heat gains, while the BIPV retrofitting cases had diverging heat balances.

The BIPV curtain wall of Option 1 had a greatly reduced solar gain compared to the baseline model. Before 8 am and after 6 pm, the internal zones of the building were losing heat to the outside environment through the low thermal resistance of the BIPV glazing as shown by the façade gain being in the negative domain at those specific hours. The BIPV-DSF of Option 4 balanced the effect of low thermal resistance of the BIPV glazing with its insulating air gap but did little to reduce on the total cooling load of the baseline building.

Even though Option 2 and Option 3 had roofs retrofitted in, there was the direct solar heat gains from existing glazing that had the biggest impact on the thermal loads. The roof heat gain was also higher than baseline for the uninsulated roof BIPV membrane (Option 2), which was losing heat to the surroundings before 9.30 am accounting for a lower heat accumulation in the building when occupancy start to increase, and HVAC air cooling requirements were decreased and thus resulted in a lower cooling demand. Option 3 (insulated roof BIPV membrane) had a net improvement on baseline and between 5:30 am and 10:30 am the heat from the internal zones was leaking outside, which was similar to Option 2 that creating a lower heat accumulation and hence a lower cooling load during occupancy.

5.3. *Building energy performance analysis*

The monthly energy consumption for each of the BIPV retrofits and the baseline building by considering all the office spaces were operational are shown in Fig. 20. Basically, all the scenarios had the similar monthly variation trend in energy across the year. On a yearly basis, the baseline building had an energy consumption of 73,349 kWh, while the retrofits of BIPV curtain wall (Option 1) and BIPV-DSF (Option 4) had energy consumptions of 79,649 kWh and 74,627 kWh respectively, which accounted for an increase of 9% and 2% over the baseline. On the other hand, the roof BIPV retrofits show less annual energy consumption in comparison with the baseline, saw 69,583 kWh and 5% less for the uninsulated roof BIPV membrane (Option 2) and 60,762 kWh and 17% less for the insulated version (Option 3). Even though the energy savings and energy excess of the different retrofit options were relatively linear compared to the baseline, it can be noticed that the histograms of BIPV-DSF (Option 4) show matching closer to the baseline especially from June to December.

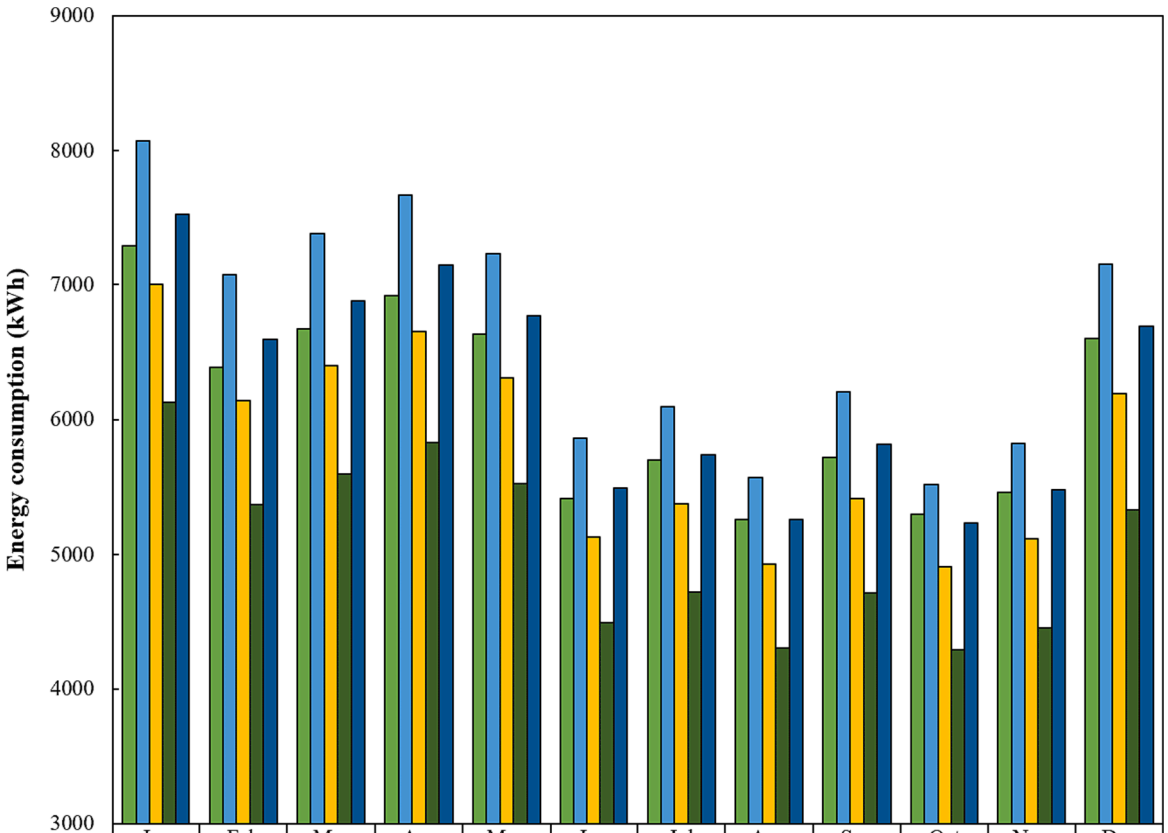

	Jan	Feb	Mar	Apr	May	Jun	Jul	Aug	Sep	Oct	Nov	Dec
Baseline	7286	6386	6671	6919	6632	5413	5700	5262	5720	5299	5461	6599
Option 1	8069	7074	7378	7661	7230	5862	6097	5571	6208	5522	5826	7153
Option 2	7004	6138	6400	6652	6310	5133	5378	4932	5417	4908	5119	6191
Option 3	6131	5373	5594	5829	5528	4491	4721	4304	4717	4289	4453	5332
Option 4	7524	6595	6881	7144	6771	5496	5741	5258	5816	5232	5480	6690

Fig. 20. Monthly energy consumption for different design options.

By extracting the cooling energy consumption from all the design options, the daily consumption distributions are shown in Fig. 21. The daily cooling energy trendlines shows that the BIPV facades required more cooling energy due to the higher heat gains, with an average increase of 12% cooling energy for the BIPV curtain wall and an average of 2% more cooling energy for the BIPV-DSF relative to the baseline. It also can be seen that the roof BIPV membrane options in overall had a better energy performance by reducing the cooling energy consumption to below the baseline case by an average of 7% and 18% for the uninsulated and insulated roof BIPV membranes, respectively.

As per the results obtained from both the dynamic building performance and the building energy performance simulations, it was found that having a lower thermal transmittance on thermal masses of the building envelope had a better effect than having a lower solar radiation transmission. Limiting the conductive heat gains with better thermal insulating materials provided by the roof BIPV membranes offers a better energy consumption factor than limiting the direct radiative heat gains provided by the BIPV facades.

By taking into account the energy generated through the BIPVs, a net resultant energy consumption for each BIPV retrofit option in comparison with the baseline case is shown in Fig. 22. It can be seen that both BIPV façade options (Option 1 and Option 4) had the monthly net energy consumption close to the baseline case, especially for the Option 1 (BIPV curtain wall), of which the monthly net energy consumption was higher than the baseline from January to September. On a yearly basis, the Option 1 had about 1.66% more net energy consumption than the baseline, while the Option 4 (BIPV-DSF) received a net energy saving of 5.16% relative to the baseline. As a result, the heat transmissions through the semi-transparent BIPV modules were apparent, but the cooling effect of BIPV-DSF would offer a degree of mitigation on the transmitted heat gains from the BIPV itself. By comparison, both roof BIPV membrane options (Option 2 and Option 3) achieved significant net energy savings of 160% and 172%, respectively; the higher energy saving from Option 3 (insulated roof BIPV membrane) demonstrated the effectiveness of the thermal insulation applied.

6. Conclusions

In this paper, a novel approach to numerically assessing the heat transfer and energy performance of BIPV was evaluated. Different BIPV retrofits in terms of thermal and energy performance for a typical office building in Mauritius were studied through finite element heat transfer analysis, dynamic building performance analysis, as well as energy performance analysis. Specifically, the BIPV retrofit options presented in this study include two BIPV façade typologies (BIPV curtain wall and BIPV-DSF) and two roof BIPV membrane typologies (uninsulated and insulated roof BIPV membranes). The results show that both BIPV facade and roof BIPV membrane options had high thermal transmission factor with their inner surfaces heated up to above 40 °C and hence created more convective heat transfer to their adjacent air (that is, the indoor air). However, the intermediate insulation panel (for the roof BIPV membrane) and the ventilated air gap (for the BIPV-DSF) showed a net reduction in the heat transfer.

The roof BIPV membranes had a better thermal performance effect

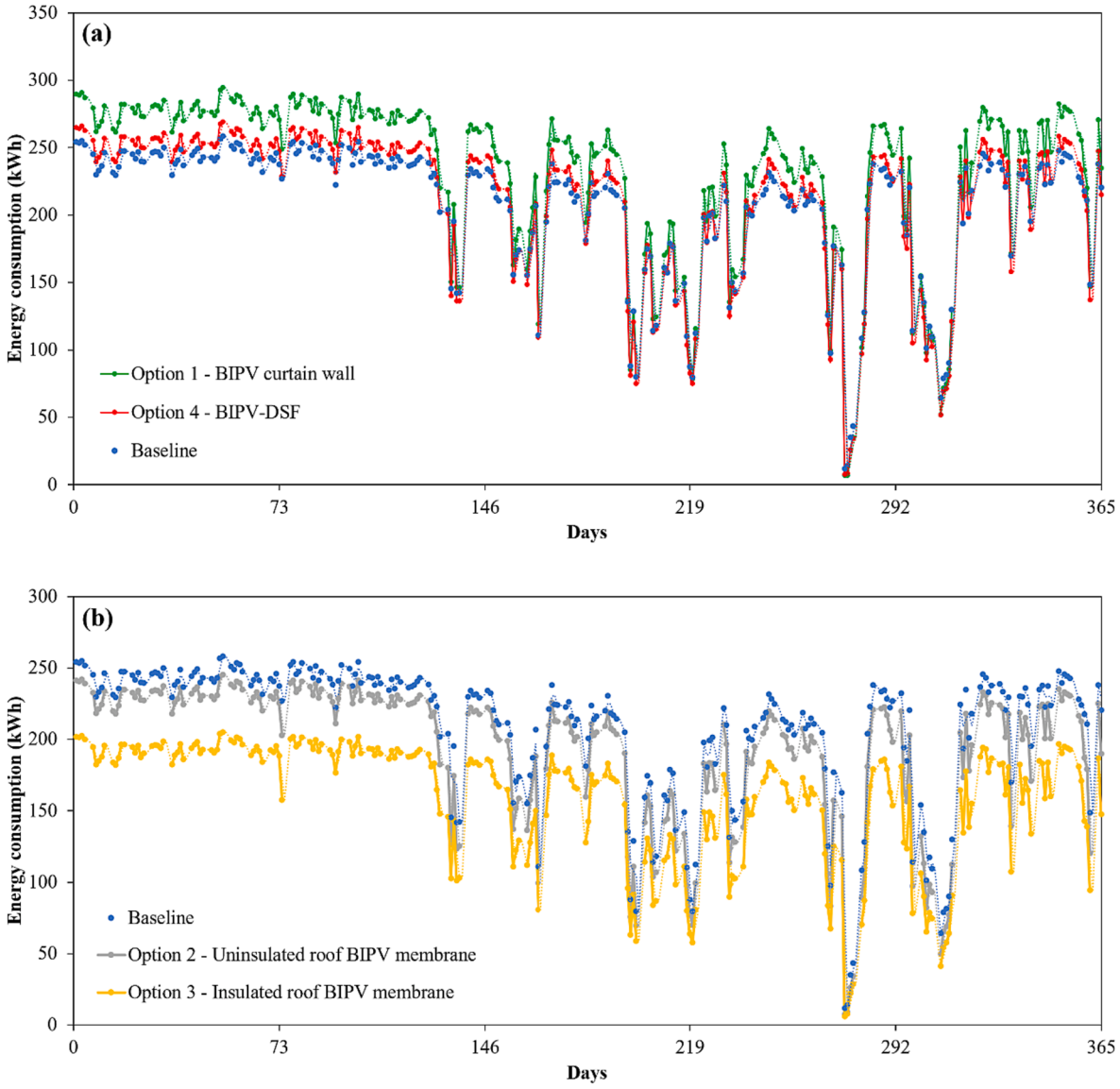

Fig. 21. Daily cooling energy consumption: (a) BIPV facades, (b) roof BIPV membrane.

on the building by reducing its cooling load by 8% for the uninsulated version and 15% for the insulated version; by contrast, both BIPV façade options could not reduce the cooling load effectively, while the BIPV curtain wall even led to an increase of cooling load for 1%. The results indicate that BIPV facades have had a negative outcome with respect to traditional construction materials for the region and climate of Mauritius, but the roof BIPV membrane whether insulated or uninsulated could help reduce the cooling load and mitigate overheating issue for the building. Furthermore, the energy analysis shows a similar outcome to the cooling load analysis with both BIPV façade options adding more energy consumption to the building (as there was 1.66% more annual energy consumption from BIPV curtain wall option), which could not be compensated by the PV electric power generated. Although the BIPV-DSF shows more promising results by reducing the net energy consumption (received a net energy saving of 5.16%), it generates too little electric power to acknowledge its viability as a low energy solution. On the other hand, both uninsulated and insulated roof BIPV membrane options achieved the annual energy saving for the building by 160% and 172%, respectively. This net positive energy balance has a strong potential towards making the building reach a net zero carbon footprint and provide a benchmark for future and existing buildings to adopt the roof BIPV membrane technology in light of their low carbon and energy efficiency performance for Mauritius and the similar climate zones.

7. Limitations and future research

Since the proposed research methodology was based solely on simulation, there was always an uncertainty factor to the outcomes of such numerical calculations although model calibration has been used to mitigate as much as possible the uncertainty and major deviations in the results. Future research should look at the actual performance of both BIPV façade and roof options through on-site experiments. Even though the roof scenario of this research was based on a roof BIPV membrane of 500 W, it should be noted that in real life applications, smaller panels would have been chosen to accommodate the actual energy consumption of the building instead of choosing the highest energy generating capacity system. Moreover, this research optimised the available space without considering actual usage of the roof space. Thus, future research should take into account the effective roof space following the building

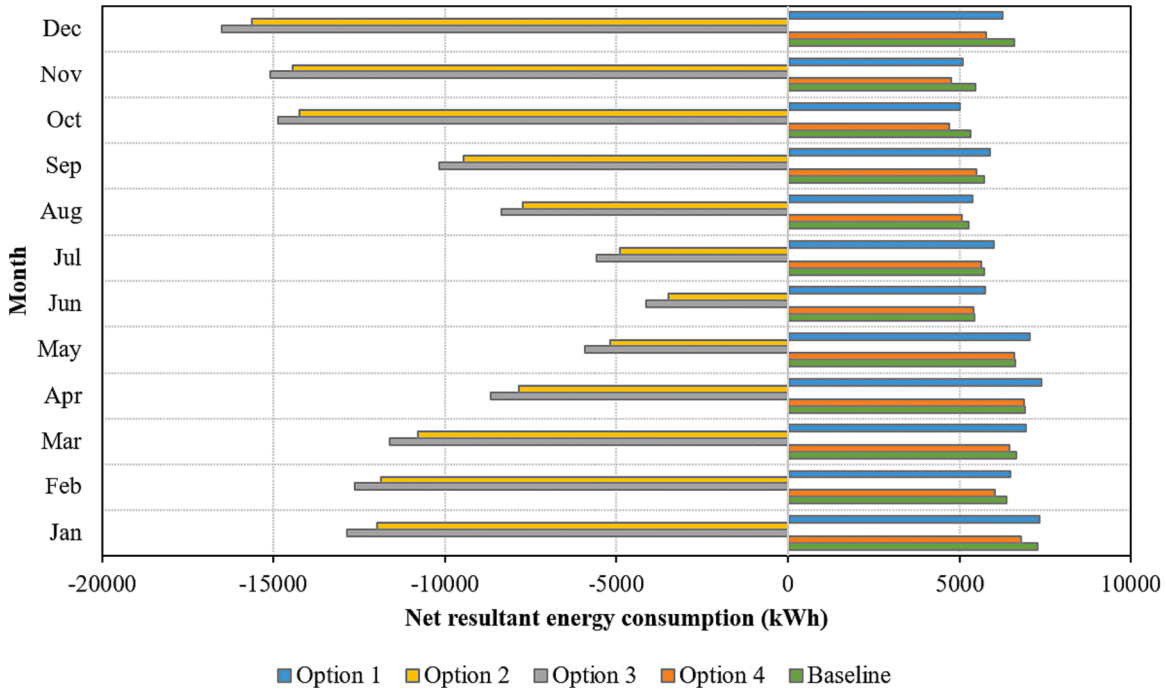

Fig. 22. Net resultant energy consumption for baseline and BIPV retrofits.

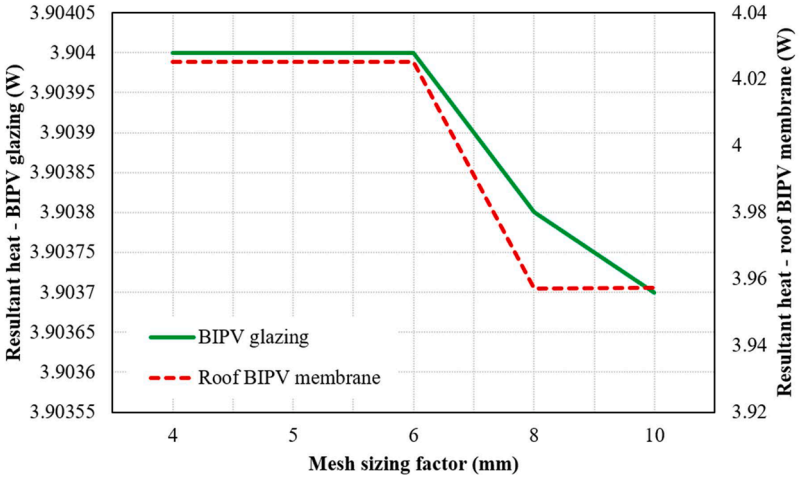

Fig. A1. Convergence between 4 mm and 10 mm mesh sizing factors for FEA.

Table A1
Mesh sizing quality metrics.

Finite element model	Sizing	Nodes	Elements	Aspect ratio	Skewness
Triple laminated glazing	4	891,165	348,785	8.15 ± 6.38	0.769 ± 0.295
Roof membrane	5	914,498	313,355	8.34 ± 6.57	0.66 ± 0.314

management plan in reality. On the other hand, this research focused on an existing office building with pre-set orientations with respect to the zenith and azimuth angles of the sun. In general, a north orientation provides better PV efficiencies in the Southern Hemisphere, while the office building in this study has a south-west orientation. This may impact on any assessment of future constructions based on this research.

CRediT authorship contribution statement

Hamza Jhumka: Methodology, Data curation, Formal analysis, Validation, Visualization, Writing – original draft. **Siliang Yang:** Conceptualization, Methodology, Supervision, Validation, Visualization, Investigation, Formal analysis, Writing – review & editing. **Christopher Gorse:** Formal analysis, Writing – review & editing. **Sara Wilkinson:** Formal analysis, Writing – review & editing. **Rebecca Yang:** Writing – review & editing. **Bao-Jie He:** Writing – review & editing. **Deo Prasad:** Writing – review & editing. **Francesco Fiorito:** Validation, Writing – review & editing.

Declaration of Competing Interest

The authors declare that they have no known competing financial interests or personal relationships that could have appeared to influence the work reported in this paper.

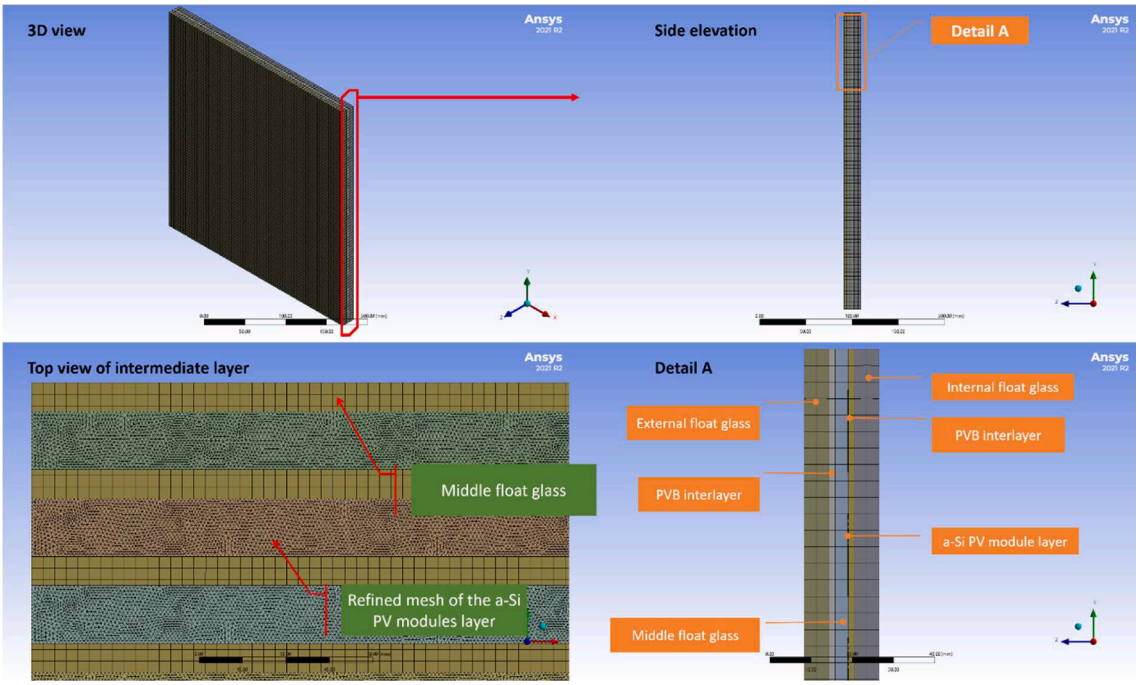

Fig. A2. Mesh refinement – triple laminated BIPV glazing.

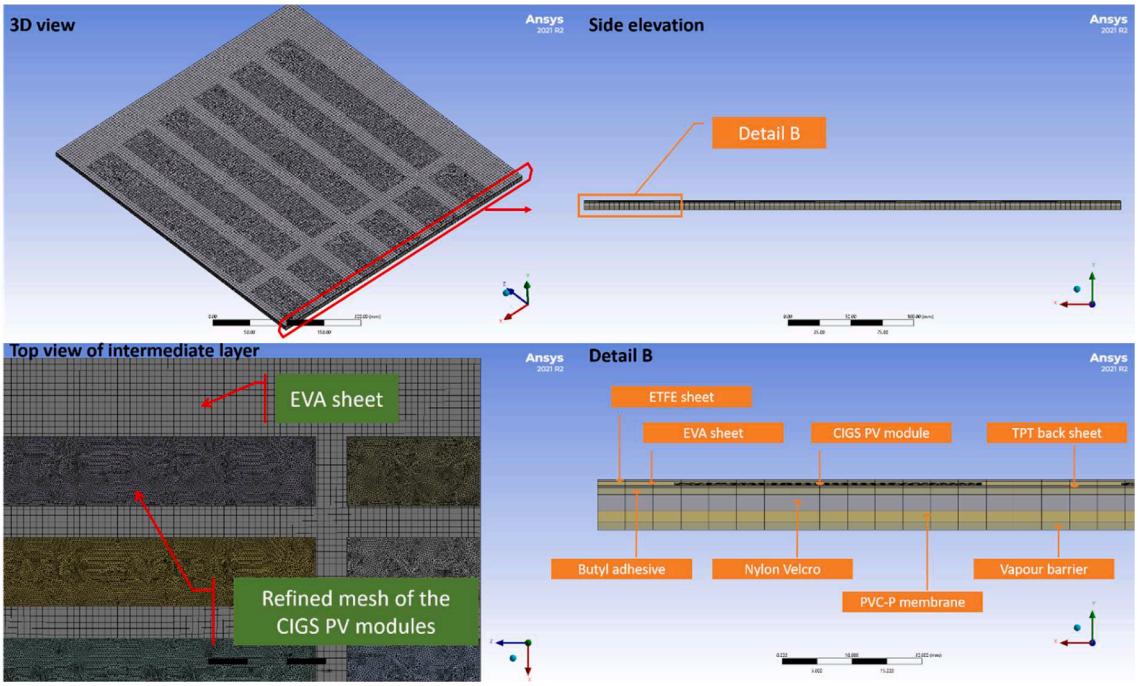

Fig. A3. Mesh refinement – roof BIPV membrane.

Data availability

Data will be made available on request.

Appendix

Appendix – Mesh refinement

Meshing is a process of sub-dividing the 3D geometry of the analysed object into a finite number of elements and nodes. With both BIPV materials and their individual components being flat and having regular shapes, a hexahedral dominant meshing type was used for the FEA of heat transfer study. To limit the processing time, smaller sections of the BIPV modules were extracted for analysis with the triple laminated BIPV glazing being reduced to a 300 mm by 320 mm section, while the roof BIPV membrane being reduced to a 425 mm by 470 mm section.

A mesh refinement was performed by reducing the mesh sizes to produce finer grids. The resultant heat emission from the inner surfaces of both FEA (BIPV glazing and roof membrane) was used as the metric to determine the optimum mesh sizing and proper results convergence.

Fig. A1 shows the convergence of both the BIPV glazing and roof BIPV membrane FEA between a 4 mm and 10 mm mesh sizing factor for the finite elements. A 4 mm mesh sizing factor was used for the triple laminated glazing and a 5 mm mesh sizing factor was used for the roof membrane with their corresponding mesh statistics and quality metrics summarised in Table A1. The PV layer was thinner than the rest of the materials encapsulating them, which was further refined with a mesh sizing factor of 2 to properly analyse the heat transitions occurring around the BIPV modules. Fig. A2 and Fig. A3 show the mesh generated for both BIPV materials using Ansys Mechanical, respectively.

References

[1] IPCC. *Climate change widespread, rapid, and intensifying*. 2022 [cited 2022 27 June]; Available from: https://www.ipcc.ch/2021/08/09/ar6-wg1-20210809-pr/.

[2] Tsang, D.C. and L. Wang, *Low Carbon Stabilization and Solidification of Hazardous Wastes*. 2021: Elsevier.

[3] M. Diesendorf, H. Saddler, Australia's polluting power: Coal-fired electricity and its impact on global warming, World Wide Fund, 2003.

[4] R. Hepple, H.u. Du, H. Feng, S. Shan, S. Yang, *Sustainability and carbon neutrality in UK's district heating: A review and analysis.* e-Prime - Advances in Electrical Engineering, Electronics and Energy 4 (2023) 100133.

[5] K. Ahmed Ali, M.I. Ahmad, Y. Yusup, Issues, impacts, and mitigations of carbon dioxide emissions in the building sector, Sustainability 12 (18) (2020) 7427.

[6] R. Hepple, S. Yang, S. Khattak, Z.i. Qian, D. Prasad, Comparative analysis of CIBSE admittance and ASHRAE radiant time series cooling load models, CivilEng 3 (2) (2022) 468–479.

[7] Economic Development Board Mauritius, *Smart City Scheme Guidelines*. 2020, Economic Development Board.

[8] United Nations Framework Convention on Climate Change (UNFCCC). *Mauritius - High-level Segment Statement COP 26*. 2021 [cited 2022 22 March]; Available from: https://unfccc.int/sites/default/files/resource/MAURITIUS_cop26cmp16cma3_HLS_EN.pdf.

[9] Board of Investment Mauritius, *Smart Mauritius - Live, Invest, Work, Play*. 2016, Board of Investment.

[10] L.-E.-E.-D.-N.-D. Moka certification to recognise Moka Smart City's commitment to sustainability, cited 2022 22 May https://www.moka.mu/en/blog/smart-solutions/leed-nd-certification-moka-sustainability/ 2022 Available from.

[11] A. Khoodaruth, V. Oree, M.K. Elahee, W.W. Clark, Exploring options for a 100% renewable energy system in mauritius by 2050, Utilities Policy 44 (2017) 38–49.

[12] A. Chel, G. Kaushik, Renewable energy technologies for sustainable development of energy efficient building, Alexandria Engineering Journal 57 (2) (2018) 655–669.

[13] United Nations Environment Programme (UNEP), Accelerating the transformational shift to a low-carbon economy in the republic of mauritius, United Nations Environment Programme, 2020.

[14] Y.K. Ramgolam, K.M.S. Soyjaudah, Unveiling the solar resource potential for photovoltaic applications in mauritius, Renewable Energy 77 (2015) 94–100.

[15] B. Ghaleb, M. Asif, Application of solar PV in commercial buildings: Utilizability of rooftops, Energy and Buildings 257 (2022) 111774.

[16] R. Trattnig, G. Cattaneo, Y. Voronko, G.C. Eder, D. Moor, F. Jamschek, T. Buchsteiner, Smart glass coatings for innovative BIPV solutions, Sustainability 13 (22) (2021) 12775.

[17] S. Yang, et al., *Study of building integrated photovoltaic/thermal double-skin facade for commercial buildings in sydney, australia*, in *Final conference of COST TU1403 "Adaptive facades network"*, Lucerne, Switzerland, 2018.

[18] E. Biyik, M. Araz, A. Hepbasli, M. Shahrestani, R. Yao, L.i. Shao, E. Essah, A. C. Oliveira, T. del Caño, E. Rico, J.L. Lechón, L. Andrade, A. Mendes, Y.B. Atlı, A key review of building integrated photovoltaic (BIPV) systems, Engineering Science and Technology, an International Journal 20 (3) (2017) 833–858.

[19] G. Yu, H. Yang, D. Luo, X.u. Cheng, M.K. Ansah, A review on developments and researches of building integrated photovoltaic (BIPV) windows and shading blinds, Renewable and Sustainable Energy Reviews 149 (2021) 111355.

[20] S. You, H. Yang, The potential electricity generating capacity of BIPV in hong kong. Conference Record of the Twenty Sixth IEEE Photovoltaic Specialists Conference-1997, IEEE, 1997.

[21] A.K. Shukla, K. Sudhakar, P. Baredar, Recent advancement in BIPV product technologies: A review, Energy and Buildings 140 (2017) 188–195.

[22] G. Ban-Weiss, C. Wray, W. Delp, P. Ly, H. Akbari, R. Levinson, Electricity production and cooling energy savings from installation of a building-integrated photovoltaic roof on an office building, Energy and Buildings 56 (2013) 210–220.

[23] R.A. Agathokleous, S.A. Kalogirou, Double skin facades (DSF) and building integrated photovoltaics (BIPV): A review of configurations and heat transfer characteristics, Renewable Energy 89 (2016) 743–756.

[24] de Wild-Scholten, M., et al. *A cost and environmental impact comparison of grid-connected rooftop and ground-based PV systems.* in *21st European Photovoltaic Solar Energy Conference*. 2006. Dresden Germany.

[25] R. Rawlings, Capturing solar energy. CIBSE Knowledge Series: KS15, Chartered Institution of Building Services Engineers, 2010.

[26] A. Ghosh, Potential of building integrated and attached/applied photovoltaic (BIPV/BAPV) for adaptive less energy-hungry building's skin: A comprehensive review, Journal of Cleaner Production 276 (2020) 123343.

[27] A. Ghosh, N. Sarmah, S. Sundaram, T.K. Mallick, Numerical studies of thermal comfort for semi-transparent building integrated photovoltaic (BIPV)-vacuum glazing system, Solar Energy 190 (2019) 608–616.

[28] F. Roberts, S. Yang, H.u. Du, R. Yang, Effect of semi-transparent a-Si PV glazing within double-skin façades on visual and energy performances under the UK climate condition, Renewable Energy 207 (2023) 601–610.

[29] P. Pal, et al., Pre-feasibility analysis and performance assessment of solar photovoltaic (PV) modules for the application of renewable power generation, Materials Today: Proceedings 39 (2021) 1813–1819.

[30] H.M. Maghrabie, M.A. Abdelkareem, A.H. Al-Alami, M. Ramadan, E. Mushtaha, T. Wilberforce, A.G. Olabi, State-of-the-Art technologies for Building-Integrated photovoltaic systems, Buildings 11 (9) (2021) 383.

[31] F. Hidayanti, The effect of monocrystalline and polycrystalline material structure on solar cell performance, International Journal of Emerging Trends in Engineering Research 8 (7) (2020) 3420–3427.

[32] K. Xiao, X. Wu, X. Song, J. Yuan, W. Bai, C. Wu, C. Huang, Study on performance degradation and damage modes of thin-film photovoltaic cell subjected to particle impact, Scientific Reports 11 (1) (2021).

[33] S. Moghadamzadeh, I.M. Hossain, T. Duong, S. Gharibzadeh, T. Abzieher, H. Pham, H. Hu, P. Fassl, U. Lemmer, B.A. Nejand, U.W. Paetzold, Triple-cation low-bandgap perovskite thin-films for high-efficiency four-terminal all-perovskite tandem solar cells, Journal of Materials Chemistry A 8 (46) (2020) 24608–24619.

[34] S. Attia, S. Bertrand, M. Cuchet, S. Yang, A. Tabadkani, Comparison of thermal energy saving potential and overheating risk of four adaptive façade technologies in office buildings, Sustainability 14 (10) (2022) 6106.

[35] S. Yang, F. Fiorito, A. Sproul, D. Prasad, Optimising design parameters of a Building-Integrated photovoltaic Double-Skin facade in different climate zones in australia, Buildings 13 (4) (2023) 1096.

[36] Pester, S., *Building-integrated photovoltaic systems: Challenges and opportunities for manufacturers and specifiers*. Information paper. 2012, Bracknell: BRE Press.

[37] J. Ramanujam, D.M. Bishop, T.K. Todorov, O. Gunawan, J. Rath, R. Nekovei, E. Artegiani, A. Romeo, Flexible CIGS, CdTe and a-Si: H based thin film solar cells: A review, Progress in Materials Science 110 (2020) 100619.

[38] Y. Yin, W. Chen, J. Hu, B. Zhao, X. Huang, Photothermal-structural-fluid behaviors of PV-ETFE cushion roof in summer: Numerical analysis using three-dimensional multiphysics model, Energy and Buildings 228 (2020) 110448.

[39] M.G.S. Conde, K. Shanks, Evaluation of available building integrated photovoltaic (BIPV) systems and their impact when used in commercial buildings in the united arab emirates, international Journal of Sustainable Energy Development (IJSED) 7 (1) (2019) 344–356.

[40] S. Yang, F. Fiorito, D. Prasad, A. Sproul, A. Cannavale, *A sensitivity analysis of design parameters of BIPV/T-DSF in relation to building energy and thermal comfort performances.* Journal of Building, Engineering 41 (2021) 102426.

[41] X. Li, J. Peng, Y. Tan, Y. He, B. Li, X. Ju, J. Ji, S. Zhang, N. Li, Y. Chen, Optimal design of inhomogeneous semi-transparent photovoltaic windows based on daylight performance and visual characters, Energy and Buildings 283 (2023) 112808.

[42] P. Boyce, N. Eklund, S. Mangum, C. Saalfield, L. Tang, Minimum acceptable transmittance of glazing, International Journal of Lighting Research and Technology 27 (3) (1995) 145–152.

[43] S. Yang, A. Cannavale, D. Prasad, A. Sproul, F. Fiorito, Numerical simulation study of BIPV/T double-skin facade for various climate zones in australia: Effects on indoor thermal comfort, Building Simulation 12 (1) (2019) 51–67.

[44] H. Sun, C.K. Heng, S.E.R. Tay, T. Chen, T. Reindl, Comprehensive feasibility assessment of building integrated photovoltaics (BIPV) on building surfaces in high-density urban environments, Solar Energy 225 (2021) 734–746.

[45] N. Rathore, N.L. Panwar, F. Yettou, A. Gama, A comprehensive review of different types of solar photovoltaic cells and their applications, International Journal of Ambient Energy 42 (10) (2021) 1200–1217.

[46] S. Yang, A. Cannavale, A. Di Carlo, D. Prasad, A. Sproul, F. Fiorito, Performance assessment of BIPV/T double-skin façade for various climate zones in australia: Effects on energy consumption, Solar Energy 199 (2020) 377–399.

[47] Yang, S., et al., *Studies on Optimal Application of Building-Integrated Photovoltaic/Thermal Facade for Commercial Buildings in Australia*, in *Proceedings of SWC2017/SHC2017*. 2017. p. 1-10.

[48] S. Yang, et al., Numerical simulation modelling of Building-Integrated photovoltaic Double-Skin facades, in: F. Bulnes, J.P. Hessling (Eds.), Recent Advances in Numerical simulations, IntechOpen, London, United Kingdom, 2021, pp. 61–75.

[49] M.A. Ekoe a Akata, D. Njomo, B. Mempouo, the effect of building integrated photovoltaic system (Bipvs) on indoor air temperatures and humidity (Iath) in the tropical region of cameroon, Future Cities and Environment 1 (0) (2015) 1.

[50] H.-M. Liu, C.-H. Young, D.-J. Horng, Y.-C. Shiue, S.-K. Lee, Improving the performance of a semitransparent BIPV by using High-Reflectivity heat insulation film, International Journal of Photoenergy 2016 (2016) 1–15.

[51] J. Han, L. Lu, J. Peng, H. Yang, Performance of ventilated double-sided PV façade compared with conventional clear glass façade, Energy and Buildings 56 (2013) 204–209.

[52] D. Sooben, N. Purohit, R. Mohee, F. Meunier, M.S. Dasgupta, R744 refrigeration as an alternative for the supermarket sector in small tropical island developing states: The case of mauritius, International Journal of Refrigeration 103 (2019) 264–273.

[53] K. Benis, I. Turan, C. Reinhart, P. Ferrão, Putting rooftops to use – A Cost-Benefit analysis of food production vs. energy generation under mediterranean climates, Cities 78 (2018) 166–179.

[54] Stolarski, T., Y. Nakasone, and S. Yoshimoto, *Engineering analysis with ANSYS software*. 2018: Butterworth-Heinemann.

[55] S. Kumar Laha, P. Kumar Sadhu, A. Ganguly, A. Kumar Naskar, A comparative study on thermal performance of a 3-D model based solar photovoltaic panel through finite element analysis, Ain Shams Engineering Journal 13 (2) (2022) 101533.
[56] Panchenko, V., S. Chirskiy, and V.V. Kharchenko, *Application of the software system of finite element analysis for the simulation and design optimization of solar photovoltaic thermal modules*, in *Handbook of Research on Smart Computing for Renewable Energy and Agro-Engineering*. 2020, IGI Global. p. 106-131.
[57] Y. Lee, A.A. Tay, Finite element thermal analysis of a solar photovoltaic module, Energy Procedia 15 (2012) 413–420.
[58] Garg, V., J. Mathur, and A. Bhatia, *Building Energy Simulation: A Workbook Using Designbuilder™*. 2020: CRC Press.
[59] Manke, P., Y.K. Garg, and V.M. Das. *Energy simulation tools and CAD interoperability: A critical review*. in *2013 International Conference on Energy Efficient Technologies for Sustainability*. 2013. IEEE.
[60] G. Elshafei, A. Negm, M. Bady, M. Suzuki, M.G. Ibrahim, Numerical and experimental investigations of the impacts of window parameters on indoor natural ventilation in a residential building, Energy and Buildings 141 (2017) 321–332.
[61] A. Fathalian, H. Kargarsharifabad, Actual validation of energy simulation and investigation of energy management strategies (Case study: An office building in semnan, iran), Case Studies in Thermal Engineering 12 (2018) 510–516.
[62] M. Baharvand, M. Hamdan, M. Abdul, DesignBuilder verification and validation for indoor natural ventilation, Journal of Basic and Applied Scientific Research (JBASR) 3 (4) (2013) 8.
[63] R.W. Lewis, P. Nithiarasu, K.N. Seetharamu (Eds.), Fundamentals of the Finite Element Method for Heat and Fluid Flow, Wiley, 2004.
[64] British Standards Institution, BS EN ISO 6946: Building components and building elements - thermal resistance and thermal transmittance - calculation method, British Standards Institution, London, 2017.
[65] U.S. Department of Energy, *EnergyPlus Version 9.6.0 Documentation* in *Engineering Reference*. 2021.
[66] ASHRAE, *Guideline 14*, in *Measurement of Energy and Demand Savings*. 2002, American Society of Heating, Refrigerating and Air-Conditioning Engineers: Atlanta, Georgia.
[67] Yang, S., *Studies on the Performances of Building Integrated Photovoltaic/Thermal Double-Skin Facade for Commercial Buildings in Australia*, in *School of Built Environment*. 2020, University of New South Wales: Sydney. p. 299.
[68] V. Sun, A. Asanakham, T. Deethayat, T. Kiatsiriroat, A new method for evaluating nominal operating cell temperature (NOCT) of unglazed photovoltaic thermal module, Energy Reports 6 (2020) 1029–1042.
[69] Jadon, A., A. Patil, and S. Jadon, *A Comprehensive Survey of Regression Based Loss Functions for Time Series Forecasting*. arXiv preprint arXiv:2211.02989, 2022.
[70] ASHRAE, *Standard 55*, in *Thermal Environmental Conditions for Human Occupancy*. 2017, American Society of Heating, Refrigerating and Air-Conditioning Engineers: Atlanta, Georgia.